Density and P-wave velocity structure beneath the Paraná Magmatic Province: refertilization of an ancient lithospheric mantle

Carlos Chaves[1, 2], Naomi Ussami[1], and Jeroen Ritsema[2]

[1]Departamento de Geofísica, Instituto de Astronomia, Geofísica e Ciências Atmosféricas, Universidade de São Paulo, Rua do Matão 1226, São Paulo, São Paulo, Brasil.

[2]Department of Earth and Environmental Sciences, University of Michigan, 2534 C. C. Little Building 1100 North University Ave, Ann Arbor, Michigan, USA.

Corresponding author: Carlos Chaves (calbertochaves@gmail.com)

Key Points:

- Density and P-wave velocity in the lithospheric mantle beneath the Paraná Magmatic Province are high.
- High density precludes a depleted cratonic lithosphere and indicates refertilized lithospheric mantle.
- Basalt magmatism suggests refertilized mantle with asthenospheric components from mantle wedge.

Abstract

We estimate density and P-wave velocity perturbations in the mantle beneath the southeastern South America plate from geoid anomalies and P-wave traveltime residuals to constrain the structure of the lithosphere underneath the Paraná Magmatic Province (PMP) and conterminous geological provinces. Our analysis shows a consistent correlation between density and velocity anomalies. The P-wave speed and density are 1% and 15 kg/m^3 lower, respectively, in the upper mantle under the Late Cretaceous to Cenozoic alkaline provinces, except beneath the Goiás Alkaline Province (GAP), where density (+20 kg/m^3) and velocity (+0.5 %) are relatively high. Underneath the PMP, the density is higher by about 50 kg/m^3 in the north and 25 kg/m^3 in the south, to a depth of 250−300 km. These values correlate with high-velocity perturbations of +0.5% and +0.3%, respectively.

Profiles of density perturbation versus depth in the upper mantle are different for the PMP and the adjacent Archean São Francisco (SFC) and Amazonian (AC) cratons. The Paleoproterozoic PMP basement has a high-density root. The density is relatively low in the SFC and AC lithospheres. A reduction of density is a typical characteristic of chemically depleted Archean cratons. A more fertile Proterozoic and Phanerozoic subcontinental lithospheric mantle has a higher density, as deduced from density estimates of mantle xenoliths of different ages and composition.

In conjunction with Re-Os isotopic studies of the PMP basalts, chemical and isotopic analyses of peridodite xenoliths from the GAP in the northern PMP, and electromagnetic induction experiments of the PMP lithosphere, our density and P-wave speed models suggest that the densification of the PMP lithosphere and flood basalt generation are related to mantle refertilization. Metasomatic refertilization resulted from the introduction of asthenospheric components from the mantle wedge above Proterozoic subduction zones, which surrounded the Paraná lithosphere. The high-density PMP lithosphere is presently gravitationally unstable and prone to delamination.

1 Introduction

The Paraná Magmatic Province (PMP) in southeastern South America and the Etendeka Magmatic Province (EMP) in Africa (Figure 1) are among the largest igneous provinces on Earth. They were formed ~134 million years ago [*Renne et al.*, 1996a, b; *Thiede and Vasconcelos*, 2010] prior to the break-up of West Gondwanaland. The duration of basalt eruptions was short, 1.5−2.0 Myr [*Renne et al.*, 1996a]. Rifting and lithosphere extension started at ~126 Ma and were accompanied by dyke intrusions along the coasts of southeastern Brazil and southwestern Africa. The final break-up created two conjugated margins comprising the Campos (CAB), Santos (SB) and Pelotas (PB) basins on the east [*Mohriak et al.*, 2002] and the Orange and Walvis basins on the west [*Bauer et al.*, 2003]. Basalts in the CAB and SB are similar in composition to the basalts of the northern PMP [*Mizusaki et al.*, 1992].

Seafloor spreading in South Atlantic started in the Albian (~113 Ma) time [*Chang et al.*, 1992] and the eruption of volcanic rocks continued around this latitude (Figure 1). The Rio Grande Rise (RGR) and the Walvis Ridge (WR) were formed at 84 Ma within the oceanic plate, initially with tholeiitic basalts and since the Middle Eocene with alkaline basalts. This gave rise to seamounts and guyots [*Gamboa and Rabinowitz*, 1984]. Because of the age progression of the WR volcanism from the African plate and its proximity to the Tristan da Cunha (TC) hotspot, both the RGR−WR and the PMP−EMP magmatic provinces have been associated with a deep mantle plume [*O'Connor and Duncan*, 1990; *Ewart et al.*, 1998]. However, this causative process has not yet been widely accepted [*Peate et al.*, 1999; *Ernesto et al.*, 2002; *Class and Roex*, 2006].

Geochemical and petrological studies on the PMP basalts [e.g. *Piccirillo et al.*, 1989; *Peate*, 1997; *Marques et al.*, 1999] indicate melting of a heterogeneous and enriched lithospheric mantle. The EMP basalts show the same compositional zonation [*Erlank et al.*, 1984] as in the PMP (> 2% high-TiO_2 content in the northern PMP and ≤ 2% low-TiO_2 content in the southern PMP). Using Os isotopic data, *Thompson et al.* [2007] proposed an asthenospheric component for the EMP basalts. This component indicates an interaction of a deeper mantle source with a metasomatized sub-continental lithospheric mantle (SCLM) prior to the formation of the basaltic magmas. Thus, this observation does not exclude the participation of a mantle plume as the source of the excess of volcanism at this latitude. On the contrary, it is invoked to explain the

PMP−EMP and the South Atlantic magmatic provinces due to plumes (TC and Gough), which compositionally evolved through time [e.g. *Gibson et al., 2005*; *Hoernle et al.*, 2015] and are now seen as a lateral volcanic manifestation of a large low velocity zone located in southern Africa [*Burke et al.*, 2008].

The TC plume as the main source of the PMP volcanism is inconsistent with paleomagnetic data. Paleogeographic reconstruction of Western Gondwanaland back to the Early Cretaceous by *Ernesto et al.* [2002] shows that the TC hotspot would be located 1,000 km south of the PMP in the onset of the flood basalts. *Rocha-Júnior et al.* [2012] measured a value of 0.1295±0.0018 for the $^{187}Os/^{186}Os$ isotope ratio of the PMP basalts. This value is much higher (0.2280) for the TC basalts, indicating that there is no link between the present-day TC melts and the PMP basalts. The Sr and Pb isotopes of tholeiites basalts samples from the RGR and WR indicate melting of SCLM rather than TC plume volcanism [see *Ernesto et al.*, 2002]. The RGR tholeiites have high concentration of TiO_2 (> 2%), similar to the northern PMP basalts and WR tholeiites have low concentration of TiO_2 (≤ 2%), similar to the southern PMP basalts. They were erupted 50 Myr after the formation of the PMP–EMP [*Gamboa and Rabinowitz*, 1984]. Thus, to decipher the origin of the PMP–EMP and the South Atlantic igneous provinces, it is essential to understand the physical properties of their SCLM from geophysical studies. In the present study, we focus primarily on the PMP.

The PMP lies almost entirely within the intracontinental Paleozoic Paraná basin. The subsidence history of this basin spans ~350 Myr before the flood basalt volcanism [*Milani and Ramos*, 1998]. During the Brasiliano/Pan-African orogeny, between 650 and 550 Ma ago, the Paraná basin was amalgamated with the neighbouring cratons (AC-Amazonian [*Tassinari and Macambira*, 1999], SFC-São Francisco [*Teixeira and Figueiredo*, 1991] and Rio de la Plata [*Rapella et al*, 2007]) by Neoproterozoic to Early Cambrian sutures (PyB – Paraguay and BB – Brasilia belts) [*Brito Neves et al.*, 1999; *Almeida et al.*, 2000].

Since the 1990s, several seismological studies have indicated that the crust beneath the PMP is thicker than 40 km [e.g., *Snoke and James*, 1997; *Feng et al.*, 2007; *Juliá et al.*, 2008] and the wave speed is relatively high in the upper mantle to a depth of 250 km [*Schimmel et al.*, 2003; *Heintz et al.*, 2005; *Feng et al.*, 2007; *Lebedev et al.,* 2009*; Rocha et al.*, 2011; *Schaeffer and Lebedev*, 2013]. These observations are typical for cratons, even though not every craton overlies high-velocity roots [e.g. *Carlson et al.*, 2005; *King*, 2005]. Heat flow in the central part of the Paraná basin ranges from 40 to 50 mWm^{-2} [*Hurter and Pollack*, 1996], being slightly above of typical heat flow in Archean regions [e.g. *Pollack and Chapman*, 1997; *Poudjom-Djomani et al.*, 2001; *Carlson et al.*, 2005], but within the typical range for Proterozoic lithosphere [*Poudjom-Djomani et al.*, 2001]. Using Rb/Sr and K/Ar methods, *Cordani et al.* [1984] dated the north-central basement of the PMP as Paleoproterozoic (2.1 Ga). This age together with gravity interpretation led *Mantovani et al.* [2005] to propose a cratonic lithosphere beneath the PMP. *Pérez-Gussinyé et al.* [2007] estimate the effective elastic thickness to be thicker than 70 km, similar to the values estimated for the Archean AC and SFC. Nevertheless, *Padilha et al.* [2015] have argued against the cratonic character of the PMP lithosphere from Geomagnetic Deep Sounding and long-period magnetotellurics. The uppermost mantle beneath the PMP has resistivity less than 500 Ωm, a value normally expected for thermally or compositionally modified lithosphere [*Eaton et al.*, 2009; *Selway*, 2014].

In the present paper, we study the geoid and new seismic data to derive density and P-wave speed perturbations in the upper mantle beneath the PMP. The combination of seismic and geoid (or gravity) data to study the upper mantle has already proven to be effective in evaluating the causes of velocity and density variations within the lithosphere, either due to composition or thermal origin [*Kaban et al.*, 2010; *Tondi et al.*, 2012; *Chaves and Ussami*, 2013; *Kaban et al.*, 2015].

We describe the geoid modeling and the resolved density structure in section 2. We discuss in some detail the constraints on the crustal structure of the region and its influence on estimating the contribution of density variations in the mantle to the geoid. In section 3, we discuss the modeling of P-wave travel time residuals and the model of P-wave speed variations in the upper mantle. In Section 4, we highlight the main characteristics of our density and P-wave models. Our results indicate that the density (+50 kg/m^3) and P-wave speed (+0.5%) beneath the PMP are both relatively high. We interpret our results using the study of *Poudjom-Dojmani et al.* [2001] where natural density estimates were obtained from peridotite xenoliths and xenocrystals of different ages. These authors found a secular variation of SCLM densities from Archean to Phanerozoic times with lower density values for depleted Archean cratonic mantle due to the intense melt extraction at the earliest stage of an Archean lithosphere formation. The density increases as the SCLM becomes younger and refertilized. For the PMP and SFC cases, the secular evolution in their SCLM composition are reinforced by the chemical and isotopic analyses of peridodite xenoliths from the Late Creatceous Goiás (GAP) and Alto Paranaíba (APAP) magmatic provinces by *Carlson et al.* [2007]. These authors found that the SCLM under the GAP is fertile, while the SCLM beneath the APAP is depleted. The APAP is underlain by the SFC lithospheric mantle. Our density and velocity models show that the density (-15 kg/m^3) and velocity (-0.5 %) beneath the APAP are relatively low. The GAP xenoliths samples are located at the northwestern edge of the PMP, where our models resolved high density (+20 kg/m^3) and high velocity (+0.5 %). Thus, the GAP xenoliths probably are samples of a refertilized PMP SCLM, which reinforces the estimates of our models.

We discuss two possible mechanisms, which could explain high density and velocity in the PMP, either by reconstructing the SCLM after lithospheric delamination or alternatively, by changing the bulk properties of the PMP lithosphere due to metasomatic refertilization of its SCLM. For the PMP case, the most likely process is the addition of melts and fluids generated at the mantle wedge above a subducting oceanic lithosphere as proposed by Re-Os and isotopic studies on the PMP basalts. The PMP basalts were extracted from partial melt of this refertilized SCLM.

2 Modeling density variations from residual geoid

2.1 Geoid data and geoid corrections

The geoid height data, ΔN_{EGM}, were calculated from the Earth Gravity Model EGM2008 [*Pavlis et al.,* 2012], which is expressed as a sum of spherical harmonics, complete up to degree and order 2159. Figures 2a and 2b show ΔN_{EGM} at spherical harmonic degree and order higher than 7 [see *Bowin*, 2000]. To isolate the geoid anomalies produced by density variations within the lower crust, the upper mantle and the uppermost lower mantle, we model geoid variations with wavelengths between 111 km and 5400 km (Figures 2c and 2d). ΔN_{EGM} varies from -13 m to +19 m within the study region. The geoid minimum of -12 m over the PMP is primarily due to the thick crust and sediment strata.

To isolate the contribution to the geoid by density anomalies in the upper mantle beneath the PMP, we make corrections to ΔN_{EGM} by discretizing models of topography, Moho depth variation, sediment and basalt into a set of tesseroids. We use the Gauss-Legendre Quadrature

(GLQ) numerical method [e.g., *Asgharzadeh et al.*, 2007; *Wild-Pfeiffer*, 2008; *Li et al.*, 2011] to calculate the effect of each tesseroid on the geoid. Figure 3 shows these effects separately.

We remove the contribution to the geoid due to topography and bathymetry using the ETOPO1 database [*Amante and Eakins*, 2009]. We filter the ETOPO1 data to a resolution of 5 arc-minutes (~9.25×9.25 km^2) consistent with the shortest wavelength (i.e., degree 2159) signal in EGM2008. We assume a density of 2670 kg/m^3 for the continental crust following *Hinze* [2003], 1030 kg/m^3 for seawater, and 2900 kg/m^3 for the oceanic crust. ΔN_{TOPO} is a long-wavelength signal and varies smoothly by about -130 m to 172 m within the study region (Figure 3a).

We determine the effect of the crust, ΔN_{CRUST} (Figure 3b), on the geoid using CRUST1.0 [*Laske et al.*, 2013] (Figure 4a) and regional constraints in the study area. CRUST1.0 is a global model of the crust discretized with lateral resolution of 1°. It represents the large-scale effects on the geoid. The regional constraints are taken from a 10'×10' crustal model (Figure 4b), which was estimated from the interpolation of compiled receiver function values of *Assumpção et al.* [2013] along with estimates of local (Airy) compensation of the observed topography from ETOPO1. These constraints are important for estimating the shortest wavelength effects on the geoid. Both CRUST1.0 and receiver function analysis by *Juliá et al.* [2008] indicate that the crust beneath the PMP is approximately 41±2 km thick. The most recent surface-wave tomography experiment by *Rosa et al.* [2016] shows that the crust beneath the Chaco-Paraná basin (CB) is, on average, 35 km thick as predicted by local compensation of the observed topography. In the northern CB, the crust thickness is about 30 km. Thus, CRUST1.0 is not compatible with regional crustal models for the CB in the southwestern part of our study area [e.g. *Snoke and James*, 1997; *Feng et al.*, 2007, *Assumpção et al.*, 2013; *Rosa et al.*, 2016]. In CRUST1.0, the crustal thickness is 40 km throughout the region. ΔN_{CRUST} is, like ΔN_{TOPO}, a predominantly long-wavelength signal. The signal varies from -85 m beneath the Andes to +330 m beneath the Atlantic Ocean. ΔN_{CRUST} has values ranging from –55 m to 180 m within the study region.

The contribution ΔN_{SEDM} (Figure 3c) to the geoid due to sediment cover originates primarily from the thick sediment strata within the Paraná, the Chaco-Paraná, and the adjacent oceanic basins. These strata are up to 6.5 km thick. ΔN_{SEDM} is as large as -60 m. ΔN_{SEDM} has significant short wavelength variations in the study region and may influence local modeling of the density structure most.

Finally, we estimate the contribution to the geoid ΔN_{BSLT} (Figure 3d) from the Serra Geral Formation (a basalt layer up to 1.5 km thick) using the isopach map from *Molina et al.* [1988] and by assuming that the density of the basalts is 2850 kg/m^3 using the work of *Marques et al.* [1984]. ΔN_{BSLT} has maximum amplitude of about +3 m.

The residual geoid anomaly, ΔN_{RES}, is obtained by subtracting from ΔN_{EGM} the contribution to the geoid from topography, crustal structure, sediment thickness variations, and the Serra Geral Formation: $\Delta N_{RES} = \Delta N_{EGM} - (\Delta N_{TOPO} + \Delta N_{CRUST} + \Delta N_{SEDM} + \Delta N_{BSLT})$. Over the PMP, the maximum amplitude of ΔN_{RES} is about +20 m (Figure 2c and 2d) where basalt layers are thickest (about 1500 m). The positive anomaly suggests that a high-density anomaly is present in the mantle beneath the PMP.

2.2 Uncertainties in the residual geoid ΔN_{RES}

Since the corrections ΔN_{TOPO}, ΔN_{CRUST}, ΔN_{SEDM}, and ΔN_{BSLT} are large compared to the residual geoid ΔN_{RES}, it is critical to evaluate the uncertainties in the corrections. Thanks to advances in satellite-derived gravity data acquisition, the accuracy of models of the geopotential has substantially improved. The geoid model EGM2008 has an accuracy of 0.15 m worldwide [see *Pavlis et al.*, 2012]. Thus, errors in ΔN_{EGM} are insignificant.

ETOPO1 for the continents is based on data from the Shuttle Radar Topography Mission. For the PMP, errors do not exceed 12 m [see *Farr et al.*, 2007]. Most of the bathymetric data in ETOPO1 are derived from the General Bathymetric Chart of the Oceans and may have errors larger than 50 m [e.g., *Marks et al.*, 2010]. If the errors in ETOPO1 are random and if the uncertainty in the assumed values for density of continental and oceanic rock is at most 10%, the estimated error of the geoid for continental South America and the southwestern Atlantic Ocean does not exceed 0.20 m and 0.70 m, respectively, for the short-wavelength (< 200 km) geoid anomalies. The effect of ETOPO1 uncertainties and uncertainties in the densities of crustal and mantle rock are even smaller for the long wavelength geoid variations that determine the density structure in the lower crust and upper mantle beneath the PMP.

The sediment structure in CRUST1.0 comprises three layers based on the compilation of *Laske and Masters* [1997]. The difference between the *Laske and Masters* [1997] model and the Mobil sediment thickness model (i.e., PLATES project) for the PMP and adjacent areas is less than 1 km [*Heine*, 2007]. We determine therefore that CRUST1.0 is a good model for the sediment structure of the study region. Assuming that the errors of sediment thickness in CRUST1.0 are random and smaller than 10% of the observed values (both thickness and density), the estimated geoid errors are typically smaller than 0.18 m, but they can be as high as 0.75 m in offshore basins such as the Pelotas basin (PB). Although these errors are small and more likely to project as short-wavelength geoid anomalies, systematic errors in sedimentary models can produce geoid anomalies of up to 3 m with an uncertainty in the mantle density model of about 10 kg/m^3.

The largest source of uncertainty in ΔN_{RES} and estimates of density perturbations in the mantle originates from crustal structure corrections since reliable seismic models of the crust depend on good station coverage [e.g. *Herceg et al.*, 2016]. Thus, it is important to evaluate how uncertainties in crustal thickness may influence the estimated density models.

Figure 5a and 5b compares ΔN_{RES} for the study area obtained from CRUST1.0 and the crustal model for the region (see Section 2.1), which will be referred to as RCM10. CRUST1.0 and RCM10 differ primarily in the estimate of the thickness of the crust beneath the CB: 40 km in CRUST1.0, and 35 km in RCM10. The difference in ΔN_{RES} for these two crustal models is as high as 40 m and the sign of ΔN_{RES} is different over the CB. However, we have confidence that ΔN_{RES} of about +20 m over the PMP is correct because both CRUST1.0 and RCM10 indicate that the crust beneath the PMP is 41 km thick. To change the sign of ΔN_{RES}, the crust beneath the PMP would have to be thinner than 33 km. Such a reduction (>8 km) is inconsistent with the seismic observations. If we assume, again, that errors in RCM10 for both Moho depth and crustal density are at most 10%, the estimated geoid errors are around 1 m for the study area. Summing the uncertainties of ΔN_{EGM}, ΔN_{TOPO}, ΔN_{CRUST}, ΔN_{SEDM}, and ΔN_{BSLT}, the overall error on ΔN_{RES} may be as high as 2.6 m. This might be associated with uncertainties in the density anomalies of up to 8 kg/m^3.

2.3 Density variations: SSA-dens model

We invert ΔN_{RES} for a density model parameterizing the density anomalies in the mantle down to 1000 km depth with 55,000 tesseroids to conform to Earth's ellipsoidal shape. One layer of 2,500 tesseroids (50×50), each 55.5×55.5 km^2, span the horizontal dimensions. The upper mantle is parameterized with 22 layers.

Since estimating the density distribution from the geoid is an underdetermined problem, we add *a priori* constraints through the Lagrange multipliers method. Following *Chaves and Ussami* [2013], we include parameter-weighting matrices to avoid solutions that preferably concentrate at shallower depths and to favor solutions that concentrate in a minimum volume [e.g., *Boulanger and Chouteau*, 2001]. The minimum volume constraint avoids the density anomaly to spread through the model, allowing us to recover density contrast values related to an anomalous source more accurately [see *Chaves and Ussami*, 2013]. In addition, we impose during the inversion that density within each tesseroid cannot be perturbed by more than 60 kg/m^3. We estimate the least-squares solution with an efficient conjugate gradient algorithm [*Hestenes and Stiefel*, 1952] following *Golub and van Loan* [1996]. The best-fitting density model (SSA-dens) (Figures 6 and 7) is obtained after 209 iterations when the RMS error of the geoid was reduced from 40.29 m to 11.15 m.

Beneath the PMP, SSA-dens model includes high-density anomalies of ~30 kg/m^3 in the lower crust and > 50 kg/m^3 in the upper mantle (Figures 6) to a depth of 250-300 km. High-density anomalies of about 15 kg/m^3 are present down to 100 km depth beneath the southern and central São Francisco Craton (SFC). SSA-dens features low-density perturbations of -20 kg/m^3 up to 350 km depth along the margins of the PMP and -15 kg/m^3 to 250 km depth beneath the Amazonian craton (AC). Density perturbations are smaller than 10 kg/m^3 within the CB.

SSA-dens model is based on homogeneous distribution of geoid data and it is more sensitive to lateral than vertical density variations. In depth, changes in the signal of density contrast of different sources will be mapped only if they generate geoid anomalies with distinct wavelength. Figure 7 (profile C-C') illustrates this for the density structure beneath the AC and SFC. Although the high-density anomaly is associated with ΔN_{RES} of +20 m over the PMP, the density perturbation beneath the SFC changes sign at 150 km depth while $\Delta N_{RES} < 0$ over the SFC.

3 Modeling of traveltimes for P-wave speed variations

3.1 P-wave traveltimes

We analyze short-period (1 Hz) P and Pn (only Pn for events with focal depths larger than 50 km) traveltimes from the International Seismological Centre (ISC) catalog and our handpicked measurements. The ISC collection combines the reprocessed EHB database from *Engdahl et al.* [1998] for events from 1964 to 2008 and the reviewed ISC bulletin data for events from 2009 to 2013. We only select events from the ISC catalogs which were recorded by at least 5 stations. Our set of handpicks measurements are made for events (1992−2012) with Mb > 5.5 recorded by 37 stations, mostly from the BL network, located within the study area. From an analysis of more than 15,000 seismograms, we select 8,415 of the highest quality measurements of the traveltimes of the P-wave that are recorded by at least five stations. From 8,415 measurements, 3,434 were recorded by stations within the study area. The combined ISC and handpicked data set has P and Pn 471,688 residuals. Although source-receiver density for the PMP is good, epicentral distance sampling and distribution of seismicity (Figure 8a) are mostly related to the Andes and Central America (Figures 8b and 8c).

Corrections for station elevation and Earth's ellipticity (the EHB database already accounts for ellipticity) are based on CRUST2.0 [*Bassin et al.*, 2000] and computed using the dynamic ray tracing software of *Tian et al.* [2007]. The corrected traveltime residuals $\delta T_{cor} = \delta T - (\delta T_{ell} + \delta T_{crust} + \delta T_{topo})$ (Figure 8d) are referenced to AK135, a 1D wave speed model for the Earth [*Kennett et al.*, 1995]. The minimum and maximum values of δT_{cor} are -8.71 s and +12.77 s. Its mean value is 0.09 s and the standard deviation is 1.66 s.

3.2 Parameterization and inverse modeling

We parameterize the P-wave speed perturbations from AK135, written as δV_P from hereon, in the mantle using 225,792 spherical cells in a volume that extends 90° in latitudinal direction and 140° in longitudinal direction. The volume includes the earthquake hypocenters, seismic stations, and ray paths to circumvent trade-offs between earthquake location and mantle velocity anomalies. The cells have uniform 1.25°×1.25° areas. The 28 spherical layers of cells increase in thickness with increasing depth from the surface to the core.

We use ray theory to relate traveltime anomalies to δV_P [e.g., *Inoue et al.*, 1990; *Inoue*, 1993]. We do not use finite-frequency theory [e.g., *Hung et al.*, 2000] since the traveltime perturbations are measured at 1 Hz. We linearize the inverse problem by assuming that the ray geometry does not significantly change when 3D wave speed variations are present in the mantle. Given model non-uniqueness, we regularize the inversion by applying norm damping and smoothness. Hence, we favor models with smooth and small δV_P [e.g. *VanDecar and Snieder*, 1994; *Montelli et al.*, 2004; *Li et al.*, 2006]. The starting model is AK135 and the best-fitting solution SSA-pvel is estimated using the iterative method LSQR [*Paige and Saunders*, 1982]. SSA-pvel (Figures 9 and 10) is obtained after 400 iterations when the standard variation of the traveltime residuals has been reduced from 1.66 s to 1.03 s (Figure 8d).

3.3 Resolution test

Although checkerboard resolution test have limitations [*Lévêque et al.*, 1993; *Rawlinson and Spakman*, 2016], we use it to illustrate modeling artifacts due to heterogeneous sampling and model damping and smoothing. Figures 11a and 11c show the retrieved velocity perturbations of a checkerboard pattern of alternating +1% and -1% velocity variations for cells of 2.5°×2.5° and 5°×5° in the study area. The checkerboard pattern is retrieved within the PMP and CB in the upper 400 km of the mantle. The low amplitudes and the elongation of the resolved checkerboard squares demonstrate that model resolution beneath the southern AC, central part of the SFC, and beneath the Santos basin (SB) and PB along the eastern Brazilian continental margin is poor due to incomplete data coverage. Thus, velocity perturbations in these regions need to be interpreted with caution. The retrieved amplitude of the velocity anomalies 0.85% for the 2.5°×2.5° cells and 0.9% for the 5°×5° cells is owing to model damping and smoothing. Hence, it is likely that amplitude of the δV_P variations is underestimated by SSA-pvel. Smearing in the NW-SE direction for δV_P variations within the PMP is due to excess of ray paths from the northwestern Andes and Central America (Figures 8b and 8c). Beneath the CB, elongations in the retrieved δV_P perturbations are related to the events from the southwestern Andes.

Rawlinson and Spakman [2016] have recently argued that spike tests are more useful than the standard checkerboard test to access the resolution of linearized tomography problems. Thus, we also perform spike tests to evaluate the ability of our raypath set to estimate the velocity structure in the study area. The spike test consists of spaced or sparse velocity variation cells. In our first spike tests (Figures 11b and 11d), we use cells of same size and amplitude of δV_P as the checkboard test in Figures 11a and 11b. Like before, the retrieved spikes in Figures 11b and 11d are better estimated within the PMP, but now with lower velocity amplitudes than in the checkboard model. *Rawlinson and Spakman* [2016] suggested that these higher amplitudes in checkboard tests are due to the proximity of neighboring cells. Lack of resolution in regions surrounding the PMP is more evident now chiefly for cells of 2.5˚×2.5˚ as well as distortions in the imaged anomalies.

Further spike tests for perturbed sparse cells of 2.5˚×2.5˚ and 3.75°×3.75° are shown in Figures S1, S2 and S3. The alternating amplitudes of δV_P perturbations are +1% and -1% and start at the surface going to 660 km depth. In the southern PMP, the high-velocity spike of 2.5˚×2.5˚ is not recovered for depths down to 310 km (Figures S1a and S2), which may indicate lack of resolution for velocity anomalies with this wavelength. For cells of 3.75˚×3.75˚, this same high-velocity spike is smeared (Figures S1b and S3). Beneath the CB, the spikes are retrieved down to 165 km, showing reduced velocity amplitudes and strong smearing. Upper mantle spikes for cells of 2.5˚×2.5˚ are only retrieved within the PMP and CB. Recovered spikes for cells of 3.75˚×3.75˚ show low amplitudes and strong distortion in the mantle beneath the AC, SB, PB and central part of the SFC.

3.4 P-wave speed variations: model SSA-pvel

Model SSA-pvel (Figures 9 and 10) indicates deep extension of high-wave speed anomalies, and it resolves velocity variations with high vertical and lateral resolution, albeit that resolution is heterogeneous and highly dependent on ray path coverage (see Figure 10).

In contrast to previously developed P-wave images of the study region [*VanDecar et al.*, 1995; *Schimmel et al.*, 2003; *Rocha et al.*, 2011], SSA-pvel is derived from absolute traveltime residuals. By earthquake relocation, we reduce the influence of erroneous source locations on the absolute residuals. Nonetheless, SSA-pvel correlates well with the images of these earlier studies. For example, SSA-pvel includes a low-velocity anomaly (δV_P = -0.6%) near the northeastern boundary of the PMP (Figure 9 and Figure 10a, profile C-C') that has been imaged previously by *VanDecar et al.*, 1995. SSA-pvel exhibits a high-velocity anomaly (δV_P = +0.6%) to the west of the PMP at depth of 500 to 800 km, which was interpreted by *Schimmel et al.* [2003] as the subducting Nazca Plate. Low-velocity perturbations are persistent along the edges of the PMP up to 400 km depth. Along the northern edge of the PMP, low-velocity anomaly is resolved beneath the alkaline province of Alto Paranaíba (APAP), while high-velocity is predicted beneath the alkaline province of Goías (GAP). A strong velocity reduction of about -1% is observed beneath the Serra do Mar Alkaline Province (SMAP) down to 165 km. *Rocha et al.* [2011] imaged the same velocity reduction but with much lower amplitude (about -0.3%). The low-velocity perturbation (about -0.7%) beneath the Ponta Grossa Arch (PGA) is better defined in our P-wave model than in the study of *Rocha et al.* [2011].

Within the PMP, SSA-pvel presents three blocks of high-velocity perturbations (about 0.5%) to a depth of 300-350 km, which were only partially recovered by previous P-wave tomography due to limited coverage. SSA-pvel also exhibits a very low wave speed anomaly (about -1%) beneath the CB, which is outside of the target volume of previous P-wave tomographic studies. This feature is in agreement with the low S-wave velocity perturbation (about -5%) from the surface-wave model of *Feng et al.* [2007].

4 Discussion

4.1 Key characteristics of SSA-dens and SSA-pvel

A quantitative comparison of SSA-dens and SSA-pvel is difficult since the models have been constructed using data with entirely different sensitivities and, hence, fundamentally different resolution. The vertical elongation of density anomalies in SSA-dens and the oblique elongation of wave speed anomalies in SSA-pvel (along ray paths), seen in Figure 10, are well-understood modeling artifacts. We have confidence however that density and P-wave speed variations in the uppermost mantle beneath the PMP are well determined. Image resolution in this part is best for both SSA-dens and SSA-pvel (see Figures 11, S1, S2 and S3) and the density and wave speed anomalies can be linked to the P-wave arrival times at seismic stations within the PMP and the residual geoid over the PMP.

In the northeastern PMP, where seismic station coverage is excellent, SSA-pvel resolves low-wave speed anomalies (between -0.4 to -1%) beneath the APAP, PGA and SMAP (Figure 9). SSA-dens resolves low-density perturbations (between -5 to -15 kg/m^3) for the APAP, PGA and SMA (Figure 5). Alkaline intrusion, fluid, chemical variations and thermal anomalies may be related to these seismic anomalies [e.g. *Assumpção et al.*, 2004; *Rocha et al.* 2011; *Bologna et al.*, 2011].

Both SSA-dens and SSA-pvel reveal a belt of relatively low-density and low-velocity around the PMP, at depths shallower than 250 km, which is only interrupted by a high-density and high-velocity structure beneath the GAP. These low-density and low-velocity anomalies correlate very well with Neoproterozoic suture zones (fold/thrust belts where the alkaline magmatism is located). The east-west elongation of the wave speed anomalies may be an imaging artifact. SSA-dens provides an image of the density variation in horizontal view with less distortion than SSA-pvel due to a more homogeneous distribution of geoid data. Lateral changes in density are directly related to lithospheric thickness and composition variations.

The low-velocity anomaly (-0.6%) in SSA-pvel in the upper mantle near the northeastern boundary of the PMP (Figure 9 and Figure 10, profile C-C') has been imaged previously as a low-velocity cylindrical structure [*VanDecar et al.*, 1995; *Schimmel et al.*, 2003; *Rocha et al.*, 2011]. In our model, this low-velocity anomaly is confined to 600 km depth. SSA-dens does not show any evidence for density perturbation where the FC is located (Figures 6 and 7, profile C-C'), which suggests that low-velocity anomaly might have chemical origin as *Rocha et al.* [2011] had already proposed.

Another striking feature in the SSA-dens model is a high-density lithospheric block in the SB, which is broader and much thicker than the PMP block. The maximum density increase is 55 kg/m^3 at a depth of 150 km and the density perturbation extends to 450 km depth. Wide-angle seismic profiles of *Evain et al.* [2015] show high-velocity within the crust and uppermost mantle beneath the SB. In Figure 5, for slices down to 150 km, a negative linear density structure separates the SB from PB, the latter also characterized by high-density.

The density and P-wave speed in the lithospheric mantle beneath the CB are relatively low (about -10 kg/m^3 and -1%, respectively). The low-speed anomaly has been resolved previously by *Snoke and James* [1997], *Feng et al.* [2007], and *Schaffer and Lebedev* [2013] and correlates very well with a low-resistivity (~ 10 Ωm) image from a magnetotelluric deep sounding by *Favetto et al.* [2015].

4.2 Densification of the PMP lithosphere

Models SSA-pvel and SSA-dens indicate high P-wave speed (+0.25−0.5%) and density perturbations (> +50 kg/m^3) beneath the central PMP to a depth of 250−300 km. Previous seismic tomography experiments have also mapped high P- and S-wave velocity in the upper mantle of the central part of the PMP [*Schimmel et al.*, 2003; *Heintz et al.*, 2005; *Feng et al.*, 2007; *Lebdev et al.*, 2009; *Rocha et al.*, 2011; *Schaeffer and Lebdev*, 2013]. The resolved high-density beneath the PMP is unexpected for Archean and Paleoproterozoic lithospheric mantle according to the analysis of mantle-derived peridotite xenoliths and garnet-xenocryst of different ages by *Poudjom-Djomani et al.* [2001], since SCLM density varies 50 kg/m^3 from Phanerozoic (mean density of 3360 kg/m^3) to Archean (mean density of 3.310 kg/m^3) due to depletion in Al, Ca and Fe.

Figure 12 shows the averaged density perturbation in the upper mantle beneath the SFC, AC, and the PMP. The PMP density profile has a maximum of +25 kg/m^3 at 100 km depth whereas the density perturbations are negative (with minima of -5 and -10 kg/m^3) for both the SFC and AC cratons. These density profiles may reflect the age-dependent compositional or thermal differences of SCLM as suggested by *Poudjom-Djomani et al.* [2001]. Cratons are thought to be stable because their negative thermal buoyancy is compensated by positive buoyancy owing to low-density, chemically depleted material [e.g. *Jordan*, 1978].

Mantle xenoliths brought by the Early Cretaceous tholeiitic basalt volcanism are absent within the PMP. Nonetheless, there are mantle xenoliths occurrences related with the Late Cretaceous mafic-alkaline in the APAP and GAP. The APAP is located between the northeastern PMP and the SFC, while the GAP is located at the northwestern PMP border (see Figure 1). According to *Carlson et al.* [2007], ^{187}Os/^{186}Os and Re-Os isotope data from the APAP peridotite xenoliths (garnet/spinel-lherzolites and spinel-harzburgites) show an average Re-depletion model ages at 2.4 Ga, indicating that these xenoliths sampled the melt depleted SCLM of the SFC. Averages of 0.2530 and 0.112335 for the Re/Os and ^{187}Os/^{186}Os ratios, respectively, as well as #Mg equals to 0.91 indicate depletion in terms of Al_2O_3 and CaO as expected for an Archean SCLM [see *O'Reilly and Griffin*, 2006]. The #Mg is the molar Mg/(Mg+Fe) ratio and reflect the inverse of the amount of Fe in peridotites. Thus, the higher the #Mg, the lower the density [see *Lee*, 2003].

The spinel-lherzolites xenoliths from the GAP, on the contrary, present averages of 0.4938 and 0.12601 for the Re/Os and $^{187}Os/^{186}Os$ ratios, respectively, and #Mg equals to 0.89. These values along with the mineral composition for Al_2O_3 (3.95%) and CaO (3.4%) plot for fertile Phanerozoic SCLM, being very close to Primitive asthenospheric mantle composition [see *O'Reilly and Griffin*, 2006]. According to *Carlson et al.* [2007], the Re-depletion model ages of this xenoliths is around 1.2 Ga, yet the age of the metasomatism is not very well constrained and it might be Middle to Neoproterozoic, connecting it to the Brasilia belt orogeny, the Goias magmatic arc evolution and the suturing of the SFC, AC and Parana lithospheres [*Pimentel and Fuck*, 1992]. The GAP xenoliths are located within the PMP where higher density is resolved by the geoid inversion (see Figure 6). Thus, the GAP xenoliths most likely are samples of the PMP SCLM.

SSA-pvel and SSA-dens analysis for the PMP and neighbouring cratons constrained by density estimates for mantle xenoliths led us to conclude that the ancient Paleoproterozoic PMP lithosphere is presently more fertile, that is, rich in denser minerals from where basalt can be extracted. The low-resistivity (< 500 Ωm) of the lithosphere beneath the PMP imaged by *Padilha et al.* [2015] also supports an altered lithosphere as typical resistivity values range between 1000 and 10000 Ωm for unaltered cratonic lithosphere [e.g. *Eaton et al.*, 2009].

4.3 Causes of densification and implications for the PMP basalts generation

Interpretation of SSA-pvel and SSA-dens for the PMP lithosphere requires a discussion regarding the causes of SCLM densification and basalt extraction. Thus, we firstly discuss the possibility of the PMP SCLM reconstruction after lithospheric delamination.

Delamination involves the foundering of a detached dense lithospheric mantle due to gravitational instability into a less dense and hot asthenosphere [*Bird*, 1979; *Elkins-Tanton and Hager*, 2000; *Lustrino*, 2005]. Both the sinking of the cold lithosphere and the rising of the hot asthenosphere may contribute to magmatic episodes [*Elkins-Tanton*, 2005; *Wang and Currie*, 2015]. Although the asthenospheric material that replaces the former lithosphere becomes depleted due melt extraction, it is more fertile in mineral composition than highly depleted peridotite of cratons, then denser. Therefore, delamination could explain the densification under the PMP. Delamination may also explain the rapid main phase of the eruption, which lasted around 1.5−2 Myr [e.g. *Renne et al.*, 1996a], the northward migration of the volcanism [*Ernesto et al.*, 1999] and the tholeiitic basalts, which are predominant type of igneous rocks in the PMP and are generated at depths shallower than 100 km. The removal of a large portion of the lithosphere affects the local isostatic equilibrium and promotes at its inception a significant uplift. For example, removing 75 km of lithosphere, at least 1 km of uplift is expect as estimated by numerical modeling [*Wang and Currie*, 2015]. However, there is no evidence for widespread uplift prior to delamination and the onset of the basaltic volcanism neither in the stratigraphic record of the Paraná basin [e.g. *Milani and Ramos*, 1998] or in the fission track (AFT) analysis of apatite in PMP basement rocks [e.g. *Gallager et al.*, 1994; *Hegarty et al.*, 1996]. Therefore, large-scale delamination of the PMP lithosphere seems to be unlikely.

An alternative densification process, which reconciles most of the geophysical, geochemical and petrological data is mantle refertilization induced by subduction of oceanic lithospheric plates during the evolution of the Paraná basin. Suture zones surround the present day PMP with convergence of the fold/thrust belts against the cratons, indicating that the subduction of an oceanic plate and its corresponding mantle wedge was located under the Paraná basin. The convective process of the asthenosphere might have contributed to basin subsidence due to dynamic topography [*Mitrovica et al.*, 1989]. At the same time, metasomatic processes changed the chemical composition and increasing the density of the SCLM above, contributing to amplify the basin subsidence. In this scenario, the model proposed by *Psysklywec and Quintas* [2000] to explain Paraná basin subsidence relating it to Panthalassa oceanic plate subduction at the Andean proto-margin should be revised.

Refertilization of the Paraná SCLM from Neoproterozoic time [*Carlson et al.*, 2007] throughout Paleozoic, culminating in the Early Cretaceous magmatism, is a plausible explanation for the increased density and velocity in the PMP lithosphere. Recent analysis of Os, Sr, Nd, and Pb isotope systematics [*Rocha-Junior et al.*, 2012, 2013] indicates that the PMP basalts were derived from a metasomatized SLCM, variably enriched in recycled components (EM-I and EM-II) and fluids released in the mantle wedge above a subducting slab. Metasomatism may have generated a veined mantle with mafic components (e.g., pyroxenites or eclogites) in the PMP. It increased mantle density and promoted partial melting due to lowering of the melting temperature by the inflow of metasomatic fluids.

5 Conclusions

The results of a new study of the density and P-wave speed in the mantle beneath the southern South America plate from a joint analysis of geoid anomalies and P-wave traveltime residuals show correlation between density (SSA-dens) and P-wave speed (SSA-pvel) anomalies beneath the Paraná Magmatic Province (PMP) and conterminous geological provinces. SSA-dens and SSA-pvel models show that the density and P-wave velocity are high beneath the PMP. The seismic structure in the central part of the PMP is typical of a cratonic lithosphere, but the high density is unexpected for ancient cratons. Compilation of density estimated of peridotite xenoliths from several subcontinental lithospheric mantle (SCLM) indicates a density decrease through time. Therefore, densification most likely occurred in the PMP during Phanerozoic ages. Geochemical and Re-Os systematic studies of the PMP basalts and the geolectrical structure of the PMP lithosphere suggest lithosphere refertilization and densification by asthenospheric components from mantle wedge at subduction zones around the Paraná lithosphere since Proterozoic times. Melting of this fertile mantle allowed large volume of basalts to be generated without increasing the temperature gradient.

Acknowledgments

Authors are grateful to an anonymous reviewer and to editor Ulrich Faul for helping to improve the manuscript. C.C. was sponsored with FAPESP (São Paulo Research Foundation) PhD (2009/18511-6) and BEPE (2013/11908-3) scholarships. N.U. was sponsored by CNPq Research Fellowship (305755/2008-0). This project was funded by FAPESP Thematic Projects (2009/50493-8). J.R. was funded by NSF (EAR-1416695). All figures were created with the GMT-Generic Mapping Tools by *Wessel and Smith* [1998]. We thank Ícaro Vitorello, Leila Marques and Eduardo Rocha-Junior for fruitful discussion. The authors acknowledge computing time provided on the Blue Gene/Q supercomputer supported by the CRC (Rice University) and LCCA (University of São Paulo) agreement. All data used in this study are available by contacting the corresponding author at calbertochaves@gmail.com.

References

Almeida, F.F.M., B.B. Brito Neves, and C. D. R. Carneiro (2000), The origin and evolution of the South American platform, Earth-Sci. Rev., 50(1–2), 77–111, doi:10.1016/S0012-8252(99)00072-0.

Amante, C., and B. W. Eakins (2009), ETOPO1 1 Arc-Minute Global Relief Model: Procedures, Data Sources and Analysis, National Geophysical Data Center, NESDIS, NOAA, U.S. Department of Commerce, Boulder, CO, August 2008.

Asgharzadeh, M. F., R. R. B. Von Frese1, H. R. Kim, T. E. Leftwich and J. W. Kim (2007), Spherical prism gravity effects by Gauss-Legendre quadrature integration, Geophysical Journal International, 169(1), 1–11, doi: 10.1111/j.1365-246X.2007.03214.x

Assumpção, M., M. Schimmel, C. Escalante, M. Rocha, J. R. Barbosa, and L. V. Barros (2004), Intraplate seismicity in SE Brazil: stress concentration in lithospheric thin spots, Geophys. J. Int, 159, 390–399, doi:10.1111/j.1365-246X.2004.02357.x.

Assumpção, M., M. B. Bianchi, J. Julià, F. L. Dias, G. S. França, R. M. Nascimento, S. Drouet, C. G. Pavão, D. F. Albuquerque, A. E. V. Lopes (2013), Crustal thickness map of Brazil: data compilation and main features, Journal of South American Earth Sciences, 43, 74-85, http://dx.doi.org/10.1016/j.jsames.2012.12.009.

Bassin, C., G. Laske, and G. Masters (2000), The Current Limits of Resolution for Surface Wave Tomography in North America, EOS Trans AGU, 81, F897.

Bauer, K., R. B. Trumbull, T. Vietor (2003), Geophysical images and a crustal model of intrusive structures beneath the Messum ring complex, Namibia, Earth and Planetary Science Letters, 216 (1–2), 65-80, http://dx.doi.org/10.1016/S0012-821X(03)00486-2.

Bird, P. (1979), Continental delamination and the Colorado Plateau, J. Geophys. Res., 84(B13), 7561–7571, doi:10.1029/JB084iB13p07561.

Brito Neves, B. B., M. C. C. Neto, and R. A. Fuck (1999), From Rodinia to Western Gondwana: An approach to the Brasiliano-Pan African Cycle and orogenic collage, Episodes, 22(3), 155-166.

Bologna, M. S., A. L. Padilha, Í. Vitorello, and M. B. Pádua (2011), Signatures of continental collisions and magmatic activity in central Brazil as indicated by a magnetotelluric profile across distinct tectonic provinces, Precambrian Res., 185, 55–64, doi:10.1016/j.precamres.2010.12.003.

Bowin, C. (2000), Mass anomaly structure of the Earth, Rev. Geophys., 38(3), 355–387, doi:10.1029/1999RG000064.

Boulanger, O., and M. Chouteau (2001), Constraints in 3D gravity inversion, Geophys. Prospect., 49(2), 265–280, doi:10.1046/j.1365-2478.2001.00254.x.

Burke, K., B. Steinberger, T. H. Torsvik, and M. A. Smethurst (2008), Plume Generation Zones at the margins of Large Low Shear Velocity Provinces on the core–mantle boundary, Earth and Planetary Science Letters, 265(1–2), 49-60, http://dx.doi.org/10.1016/j.epsl.2007.09.042.

Carlson, R. W., D. G. Pearson, and D. E. James (2005), Physical, chemical, and chronological characteristics of continental mantle, Rev. Geophys., 43, RG1001, doi:10.1029/2004RG000156.

Carlson, R. W., A. L. N. Araújo, T. C. Junqueira-Brod, J. C. Gaspar, J. A. Brod, I. A. Petrinovic, M. H. B. M. Hollanda, M. M. Pimentel, and S. Sichel (2007), Chemical and isotopic relationships between peridotite xenoliths and mafic–ultrapotassic rocks from Southern Brazil, Chemical Geology, 242(3–4), 415-434, http://dx.doi.org/10.1016/j.chemgeo.2007.04.009.

Chang, H. K., R. O. Kowsmann, A. M. F. Figueiredo, and A. Bender (1992), Tectonics and stratigraphy of the East Brazil Rift system: An Overview, Tectonophysics, 213(1–2), 97-138, http://dx.doi.org/10.1016/0040-1951(92)90253-3.

Chaves, C. A. M., and N. Ussami (2013), Modeling 3-D density distribution in the mantle from inversion of geoid anomalies: Application to the Yellowstone Province, J. Geophys. Res. Solid Earth, 118, 6328–6351, doi: 10.1002/2013JB010168.

Class, C., and A. P. Roex (2006), Continental material in the shallow oceanic mantle - How does it get there?, Geology, 34, 129–132, doi: 10.1130/G21943.1.

Cordani, U. G., B. B. Brito Neves, R. A. Fuck, R. Porto, A. Thomas Filho, and F. M. B. Cunha (1984), Estudo preliminar de integração do pré-Cambriano com os eventos tectônicos das bacias sedimentares Brasileiras, Bul. Cienc. Tec. Pet. Seção Explor. Pet., 70.

Eaton, D. W., F. Darbyshire, R. L. Evans, H. Grütter, A. G. Jones, and X. Yuan (2009), The elusive lithosphere–asthenosphere boundary (LAB) beneath cratons, Lithos, 109(1–2), 1-22, http://dx.doi.org/10.1016/j.lithos.2008.05.009.

Elkins-Tanton, Linda T., B. H. Hager (2000), Melt intrusion as a trigger for lithospheric foundering and the eruption of the Siberian flood basalts, Geophysical Research Letters : 27, 3937-3940, http://dx.doi.org/10.1029/2000GL011751.

Elkins-Tanton, L. T. (2005), Continental magmatism caused by lithospheric delamination, in Plates, Plumes, and Paradigms, edited by G. R. Foulger, J. H. Natland, D. C. Presnall, and D. L. Anderson, pp. 449-461, Geological Society of America.

Engdahl, E.R., Van der Hilst, R.D., and Buland, R.P. (1998), Global teleseismic earthquake relocation from improved travel times and procedures for depth determination, Bulletin Seismological Society of America, 88, 722-743.

Erlank, A.J., J. S. Marsh, A. R. Duncan, R. M. Miller, C. J. Hawkesworth, P. J. Betton, and D. C. Rex (1984), Geochemistry and petrogenesis of the Etendeka volcanic rocks from SWA/Namibia, in Petrogenesis of Volcanic Rocks of the Karoo province, vol. 13, edited by A. J. Erlank, pp. 195-246, Special Publication of the Geological Society of South Africa.

Ernesto, M., M. I. B Raposo, L. S Marques, P. R Renne, L. A Diogo, A de Min (1999), Paleomagnetism, geochemistry and $^{40}Ar/^{39}Ar$ dating of the North-eastern Paraná Magmatic Province: tectonic implications, Journal of Geodynamics, 28(4–5), 321-340, http://dx.doi.org/10.1016/S0264-3707(99)00013-7.

Ernesto, M, L. Marques, E. Piccirilo, E. Molina, N. Ussami, P. Cominchiaramonti, G. Bellieni (2002), Paraná Magmatic Province Tristan da Cunha plume system: fixed versus mobile plume, petrogenetic considerations and alternative heat sources, Journal of Volcanology and Geothermal Research, 118(1–2), 15-36, http://dx.doi.org/10.1016/S0377-0273(02)00248-2.

Evain, M., et al. (2015), Deep structure of the Santos Basin-São Paulo Plateau System, SE Brazil, J. Geophys. Res. Solid Earth, 120, 5401–5431, doi:10.1002/2014JB011561.

Ewart, A., Milner,S.C., Armstrong,R.A., Duncan,A.R. (1998), Etendeka Volcanism of the Goboboseb Mountains and Messum Igneous Complex, Namibia. Part I: Geochemical Evidence of Early Cretaceous Tristan Plume Melts and the Role of Crustal Contamination in the Paraná–Etendeka CFB, J. Petrology, 39(2), 191-225, doi:10.1093/petroj/39.2.191, J.Petrol.39.

Farr, T. G., et al. (2007), The Shuttle Radar Topography Mission, Rev. Geophys., 45, RG2004, doi:10.1029/2005RG000183.

Favetto A., V. Rocha, C. Pomposiello, R. García, and H. Barcelona (2015), A new limit for the NW Río de la Plata Craton Border at about 24˚S (Argentina) detected by Magnetotellurics, Geologica Acta, 13(3), 243-254, doi: 10.1344/GeologicaActa2015.13.3.6.

Feng, M., S. Van der Lee, and M. Assumpção (2007), Upper mantle structure of South America from joint inversion of waveforms and fundamental mode group velocities of Rayleigh waves, Journal of Geophysical Research, 112, B04312. http://dx.doi.org/10.1029/2006JB004449.

Gallagher, K., C. J. Hawkesworth, and M. S. M. Mantovani (1994), The denudation history of the onshore continental margin of SE Brazil inferred from apatite fission track data, J. Geophys. Res., 99(B9), 18117–18145, doi:10.1029/94JB00661.

Gamboa, L. A. P., and P. D. Rabinowitz (1984), Research on the Vema Channel The evolution of the Rio Grande Rise in the southwest Atlantic Ocean, Marine Geology, 58(1), 35-58, http://dx.doi.org/10.1016/0025-3227(84)90115-4.

Gibson S. A., R. N. Thompson, J. A. Day, S. E. Humphris, and A. P. Dickin (2005), Melt-generation processes associated with the Tristan mantle plume: Constraints on the origin of EM-1, Earth and Planetary Science Letters, 237 (3–4), 744-767, http://dx.doi.org/10.1016/j.epsl.2005.06.015.

Golub, G. H., C. F. Van Loan (1996), Matrix Computations, 694 pp., Johns Hopkins University Press, Baltimore, Maryland.

Hegarty, K. A., I. R. Duddy, and P. F. Green (1996), The thermal history in around the Paraná Basin using apatite fission track analysis - implications for hydrocarbon occurrences and basin formation, in Alkaline Magmatism in Central-Eastern Paraguay: Relationships with Coeval Magmatism in Brazil, edited by P. Comin-Chiaramonti, and C. B. Gomes, pp. 67-8, Edusp-Fapesp, São Paulo, São Paulo.

Heine, C. (2007), Formation and Evolution of intracontinental basins, PhD Thesis, School of Geosciences, The University of Sydney, Australia, unpublished.

Heintz, M., E. Debayle, and A. Vauchez (2005), Upper mantle structure of the South American continent and neighboring oceans from surface wave tomography, Tectonophysics, 406, 115–139, doi:10.1016/j.tecto.2005.05.006.

Herceg, M., I. M. Artemieva, and H. Thybo (2016), Sensitivity analysis of crustal correction for calculation of lithospheric mantle density from gravity data, Geophys. J. Int. 204 (2): 687-696 doi:10.1093/gji/ggv431

Hestenes, M. R., and E. Stiefel (1952), Methods of Conjugate Gradients For Solving Linear Systems, Journal of Research of National Bureau of Standards, 49 (6), 409-436.

Hinze, W. J. (2003), Bouguer reduction density, why 2.67?, Geophysics, 68(5), 1559, doi:10.1190/1.1620629.

Hoernle, K., J. Rohde, F. Hauff, D. Garbe-Schönberg, S. Homrighausen, R. Werner, and J. P. Morgan (2015), How and when plume zonation appeared during the 132 Myr evolution of the Tristan Hotspot, Nature Communications, 6, doi:10.1038/ncomms8799.

Hung, S.-H., F.A. Dahlen, and G. Nolet (2000), Fréchet kernels for finite-frequency traveltimes—II. Examples. Geophysical Journal International, 141, 175–203. doi: 10.1046/j.1365-246X.2000.00072.x

Hurter, S. J., and H. N. Pollack (1996), Terrestrial heat flow in the Paraná Basin, southern Brazil, J. Geophys. Res., 101, 8659–8671, doi:10.1029/95JB03743.

Inoue, H., Y. Fukao, K. Tanabe, and Y. Ogata (1990), Whole mantle P-wave travel time tomography, Physics of the Earth and Planetary Interiors, 59(4), 294-328, http://dx.doi.org/10.1016/0031-9201(90)90236-Q.

Inoue, H. (1993), Teleseismic tomography: global modeling, in Seismic Tomography: Theory and Applications, edited by H. M. Iyer and K. Hirahara, Chapman and Hall, London.

Jordan, T. H. (1978), Composition and development of the continental tectosphere, Nature 274, 544-548, doi:10.1038/274544a0.

Julià, J., M. Assumpção, and M. P. Rocha, (2008), Deep crustal structure of the Paraná Basin from receiver functions and Rayleigh-wave dispersion: evidence for a fragmented cratonic root, J. geophys. Res., 113, B08318, doi:10.1029/2007JB005374.

Kaban, M. K., M. Tesauro, S. Cloetingh (2010), An integrated gravity model for Europe's crust and upper mantle, Earth and Planetary Science Letters, 296(3-4), 195-209, doi:10.1016/j.epsl.2010.04.041.

Kaban, M. K., W. Mooney, and A. G. Petrunin (2015), Cratonic root beneath North America shifted by basal drag from the convecting mantle, Nature Geoscience 8, 797–800, doi:10.1038/ngeo2525

King, Scott D. (2005), Archean cratons and mantle dynamics. Earth and Planetary Science Letters, 234(1–2), 1-14, http://dx.doi.org/10.1016/j.epsl.2005.03.007.

Kennett, B. L. N., E. R. Engdahl, and R. Buland (1995), Constraints on seismic velocities in the Earth from traveltimes, Geophys. J. Int., 122(1), 108-124, doi:10.1111/j.1365-246X.1995.tb03540.x

Laske, G., and G. Masters (1997), A Global Digital Map of Sediment Thickness, EOS Trans. AGU, 78, F483.

Laske, G., G. Masters, Z. Ma, and M. Pasyanos (2013), Update on CRUST1.0 - A 1-degree Global Model of Earth's Crust, paper presented at Geophys. Res. Abstracts, EGU, Vienna.

Lebedev, S., J. Boonen, J. Trampert (2009), Seismic structure of Precambrian lithosphere: New constraints from broadband surface-wave dispersion, Lithos, Special Issue "Continental Lithospheric Mantle: the Petro-Geophysical Approach", 109 (1-2), 96-111, 10.1016/j.lithos.2008.06.010

Lee, C.-T. A., Compositional variation of density and seismic velocities in natural peridotites at STP conditions: Implications for seismic imaging of compositional heterogeneities in the upper mantle, J. Geophys. Res., 108(B9), 2441, doi:10.1029/2003JB002413, 2003.

Lévěque, J.-J., L. Rivera, and G. Wittlinger (1993), On the use of the checker-board test to assess the resolution of tomographic inversions, Geophysical Journal International, 115, 313–318, doi: 10.1111/j.1365-246X.1993.tb05605.x

Li, C., R. D. Van der Hilst, and N. M. Toksoz (2006), Constraining spatial variations in P-wave velocity in the upper mantle beneath SE Asia, Physics of the Earth and Planetary Interiors, 154, 180-195, doi:10.1016/j.pepi.2005.09.008.

Li, Z., T. Hao, Y. Xu, and Y. Xu (2011), An efficient and adaptive approach for modeling gravity effects in spherical coordinates, Journal of Applied Geophysics, 73(3), 221-231, http://dx.doi.org/10.1016/j.jappgeo.2011.01.004.

Lustrino, M. (2005), How the delamination and detachment of lower crust can influence basaltic magmatism, Earth-Science Reviews, 72(1–2), 21-38, http://dx.doi.org/10.1016/j.earscirev.2005.03.004.

Mantovani, M. S. M., M. C. L. Quintas, W. Shukowsky, and B. B. Brito Neves (2005), Delimitation of the Paranapanema block: A geophysical contribution, Episodes, 28, 18– 22.

Marks, K. M., W. H. F. Smith, and D. T. Sandwell, (2010) Evolution of errors in the altimetric bathymetry model used by Google Earth and GEBCO, Mar Geophys Res, 31, 223–238, doi:10.1007/s11001-010-9102-0

Marques, L.S., A. J. R. Nardi, P. P. P. Pinese, and M.I.B. Raposo (1984), Correlação entre densidade e equimismo dos principais litotipos vulcânicos da Bacio do Paraná, Presented at the 33rd Congresso Brasileiro de Geologia, Rio de Janeiro, p. 253.

Marques, L. S., B. Dupré, E. M. Piccirillo (1999), Mantle source compositions of the Paraná magmatic province: evidence from trace element and Sr–Nd–Pb isotope geochemistry, J. Geodynam, 28 (4–5), 439-458, http://dx.doi.org/10.1016/S0264-3707(99)00020-4.

Milani, E. J., and V. Ramos (1998), Orogenias paleozóicas no domínio sul-ocidental do Gondwana e os ciclos de subsidência da Bacia do Paraná, Rev. Bras. Geoc., 28(4): 527-544.

Mitrovica, J. X., C. Beaumont, and G. T. Jarvis (1989), Tilting of continental interiors by the dynamical effects of subduction, Tectonics, 8(5), 1079–1094, doi:10.1029/TC008i005p01079.

Mizusaki, A. M. P., R. Petrini, G. Bellieni, P. Comin-Chiaramonti, J. Dias, A. De min, and E. M. Piccirillo (1992), Basalt magmatism along the passive continental margin of SE Brazil (Campos Basin), Contribution to Mineralogy and Petrology, 111(2), 143-160, doi: 10.1007/BF00348948.

Mohriak, W. U., B. R. Rosendahl, J. P. Turner, and S. C. Valente (2002), Crustal architecture of South Atlantic volcanic margins, in Volcanic Rifted Margins, Geological Society of

America Special Paper, vol. 362, edited by M.A Menzies et al., pp. 159–202, Boulder, Colorado,

Molina, E.C., N. Ussami, N. C. de Sá, D. Blitzkow, O. F. Miranda-Filho (1988), Deep crustal structure under the Paraná basin (Brazil) from gravity study, in The Mesozoic Flood Volcanics of the Paraná Basin: Petrogenic and Geophysical Aspects, edited by E.M. Piccirillo and A. J. Melfi, pp. 271-283 , Universidade de São Paulo, Instituto Astronômico e Geofísico.

Montelli R., G. Nolet, G. Masters, F. A. Dahlen, and S. -H. Hung (2004), Global P and PP traveltime tomography: rays versus waves, Geophys. J. Int. 158, 637–654, doi: 0.1111/j.1365-246X.2004.02346.x

O'Connor, J. M., and R. A. Duncan (1990), Evolution of the Walvis Ridge-Rio Grande Rise Hot Spot System: Implications for African and South American Plate motions over plumes, J. Geophys. Res., 95(B11), 17475–17502, doi:10.1029/JB095iB11p17475.

O'Reilly, S. Y., and W. L. Griffin (2006), Imaging global chemical and thermal heterogeneity in the subcontinental lithospheric mantle with garnets and xenoliths: Geophysical implications, Tectonophysics, 416 (1-2), 289-309, doi: 10.1016/j.tecto.2005.11.014

Padilha, A. L., Í. Vitorello, C. E. Antunes, and M. B. Pádua (2015), Imaging three-dimensional crustal conductivity structures reflecting continental flood basalt effects hidden beneath thick intracratonic sedimentary basin, J. Geophys. Res. Solid Earth, 120, 4702–4719, doi:10.1002/2014JB011657.

Paige, C. C., and M. A. Saunders (1982), LSQR: An algorithm for sparse linear equations and sparse least squares, TOMS 8(1), 43-71.

Pavlis, N. K., S. A. Holmes, S. C. Kenyon, and J. K. Factor (2012), The development and evaluation of the Earth Gravitational Model 2008 (EGM2008), J. Geophys. Res., 117, B04406, doi:10.1029/2011JB008916.

Peate, D. W. (1997), The Paraná-Etendeka Province, in Large Igneous Provinces; Continental, Oceanic, and Planetary Flood Volcanism, Geophysical Monographs, vol. 100, edited by J. J. Mahoney and M. E. Coffin, pp. 217-245, AGU, Washington, D. C.

Peate, D., C. J. Hawkesworth, M. S. M. Mantovani, N. W. Rogers, and S. P. Turner (1999), Petrogenesis and stratigraphy of the high-Ti/Y Urubici magma type in the Paraná flood basalt province and implications for the nature of 'Dupal'-type mantle in the South Atlantic Region, Journal of Petrology, 40, 451-473, doi: 10.1093/petroj/40.3.451

Pérez-Gussinyé, M., A. R. Lowry, and A. B. Watts (2007), Effective elastic thickness of South America and its implications for intracontinental deformation, Geochem. Geophys. Geosyst., 8, Q05009, doi:10.1029/2006GC001511.

Piccirillo, E. M., L. Civetta, R. Petrini, A. Longinelli, G. Bellieni, P. Comin-Chiaramonti, L. S. Marques, and A. J. Melfi (1989), Regional Variations Within The Parana Flood Basalts (Southern Brazil): Evidence For Subcontinental Mantle Heterogeneity And Crustal Contamination, Chemical Geology, 75(1–2), 103-122, http://dx.doi.org/10.1016/0009-2541(89)90023-5.

Pimentel, M. M., and R. A. Fuck (1992), Neoproterozoic crustal accretion in central Brazil, Geology, 20, 375-379, doi:10.1130/0091-7613

Pollack, H. N., and D. S. Chapman (1977), On the regional variation of heat flow, geotherms and the thickness of the lithosphere. Tectonophysics, 38(3-4), 279-296, doi: 10.1016/0040-1951(77)90215-3.

Poudjom-Djomani, Y. H., S. Y. O'Reilly, W. L. Griffin, and P. Morgan (2001), The density structure of subcontinental lithosphere through time, Earth and Planetary Science Letters, 184 (3–4), 605-621, http://dx.doi.org/10.1016/S0012-821X(00)00362-9.

Pysklywec, R. N., and M. C. L. Quintas (2000), A mantle flow mechanism for the late Paleozoic subsidence of the Paraná Basin, J. Geophys. Res., 105(B7), 16359–16370, doi:10.1029/2000JB900080.

Rapela, C.W., R. J. Pankhurst, C. Casquet, C. M. Fanning, E. G. Baldo, J. M. González-Casado, C. Galindo, and J. Dahlquist (2007) The Río de la Plata craton and the assembly of SW Gondwana. Earth-Science Reviews, 83, 49-82, doi: 10.1016/j.earscirev.2007.03.004

Rawlinson, N. and W. Spakman (2016), On the use of sensitivity tests in seismic tomography, Geophys. J. Int., 205(2), 1221-1243, doi:10.1093/gji/ggw084

Renne, P.R., K. Deckart, M. Ernesto, G. Féraud, and E. M. Piccirillo (1996a), Age of the Ponta Grossa dike swarm (Brazil), and implications to Paraná flood volcanism: Earth and Planetary Science Letters, 144, 199–211, doi: 10.1016/0012-821X(96)00155-0.

Renne, P. R., J. M. Glen, S. C. Milner, and A. R. Duncan (1996b), Age of Etendeka flood volcanism and associated intrusions in southwestern Africa, Geology, 24, 659-662, doi:10.1130/0091-7613(1996)024.

Rocha, M. P., M. Schimmel, and M. Assumpção (2011), Upper-mantle seismic structure beneath SE and Central Brazil from P- and S-wave regional traveltime tomography, Geophysical Journal International, 184, 268–286. doi: 10.1111/j.1365-246X.2010.04831.x.

Rocha-Junior, E. V., I. S. Puchtel, L. S. Marques, R. J. Walker, F. B. Machado, A. J. R. Nardy, M. Babinski, A. M. G. Figueiredo (2012), Re-Os isotope and highly siderophile element systematics of the Paraná continental flood basalts (Brazil), Earth and Planetary Science Letters, 337–338, 164-173, http://dx.doi.org/10.1016/j.epsl.2012.04.050.

Rocha-Junior, E. R.V., L. S. Marques, M. Babinski, A. J. R. Nardy, A. M. G. Figueiredo, and F. B. Machado (2013), Sr-Nd-Pb isotopic constraints on the nature of the mantle sources involved in the genesis of the high-Ti tholeiites from northern Paraná Continental Flood Basalts (Brazil), Journal of South American Earth Sciences, 46, 9-25, http://dx.doi.org/10.1016/j.jsames.2013.04.004.

Rosa, M. L., B. Collaço, M. Assumpção, N. Sabbione, and G. Sánchez (2016), Thin crust beneath the Chaco-Paraná Basin by surface-wave tomography, Journal of South American Earth Sciences, 66, 1-14, http://dx.doi.org/10.1016/j.jsames.2015.11.010.

Schaeffer, A. J., and S. Lebedev (2013), Global shear-speed structure of the upper mantle and transition zone, Geophys. J. Int., 194(1): 417-449, doi: 10.1093/gji/ggt095.

Schimmel, M., M. Assumpção, and J. C. VanDecar (2003), Seismic velocity anomalies beneath SE Brazil from P and S wave travel time inversions, J. Geophys. Res., 108(B4), 2191, doi:10.1029/2001JB000187.

Selway, K. (2014), On the Causes of Electrical Conductivity Anomalies in Tectonically Stable Lithosphere, Surveys in Geophysics, 35 (1), 219-257, doi:10.1007/s10712-013-9235-1.

Snoke, J. A., and D. E. James (1997), Lithospheric structure of the Chaco and Paraná Basins of South America from surface-wave inversion, J. Geophys. Res., 102(B2), 2939–2951, doi:10.1029/96JB03180.

Tassinari, C. C.G. and M. J.B. Macambira (1999), Geochronological provinces of the Amazonian Craton, Episodes, 22(3), 174-182.

Teixeira, W., and M. C. H. Figueiredo (1991), An outline of Early Proterozoic crustal evolution in the São Francisco craton, Brazil: a review, Precambrian Research, 53(1), 1-22, http://dx.doi.org/10.1016/0301-9268(91)90003-S.

Thiede, D.S., and P. M. Vasconcelos (2010), Paraná flood basalts: rapid extrusion hypothesis confirmed by new $^{40}Ar/^{39}Ar$ results, Geology 38 (8), 747–750, doi: 10.1130/G30919.1.

Thompson, R.N., A. J. V. Riches, P. M. Antoshechkina, D. G. Pearson, G. M. Nowell, C. J. Ottley, A. P. Dickin, V. L. Hards, A. -K. Nguno, and V. Niku-Paavola (2007), Origin of CFB magmatism: Multi-tiered intracrustal picrite-rhyolite magmatic plumbing at Spitzkoppe, Western Namibia, during early cretaceous Etendeka magmatism, Journal of Petrology, 48 (6), 1119-1154. doi: 10.1093/petrology/egm012

Tian, Y., S.-H. Hungb, G. Nolet, R. Montelli, and F.A. Dahlen (2007), Dynamic ray tracing and traveltime corrections for global seismic tomography, Journal of Computational Physics, 226(1), 672-687, http://dx.doi.org/10.1016/j.jcp.2007.04.025.

Tondi, R., R. Schivardi, I. Molinari, and A. Morelli (2012), Upper mantle structure below the European continent: Constraints from surface-wave tomography and GRACE satellite gravity data, J. Geophys. Res., 117, B09401, doi:10.1029/2012JB009149.

VanDecar, J. C., and R. Snieder (1994), Obtaining smooth solutions to large, linear, inverse problems, Geophysics, 59(5), 818-829, doi: 10.1190/1.1443640.

VanDecar, J. C., D. E. James, and M. Assumpção (1995), Seismic evidence for a fossil mantle plume beneath South America and implications for plate driving forces, Nature, 378, 25-31, doi:10.1038/378025a0.

Wang, H., and C. A. Currie (2015), Magmatic expressions of continental lithosphere removal, J. Geophys. Res. Solid Earth, 120, doi:10.1002/ 2015JB012112.

Wessel, P., and W. H. F. Smith (1998), New improved version of the Generic Mapping Tools released, Eos Trans. AGU, 79, 579.

Wild-Pfeiffer, F. (2008), A comparison of different mass elements for use in gravity gradiometry, Journal of Geodesy, 82(10), 637-653, doi:10.1007/s00190-008-0219-8.

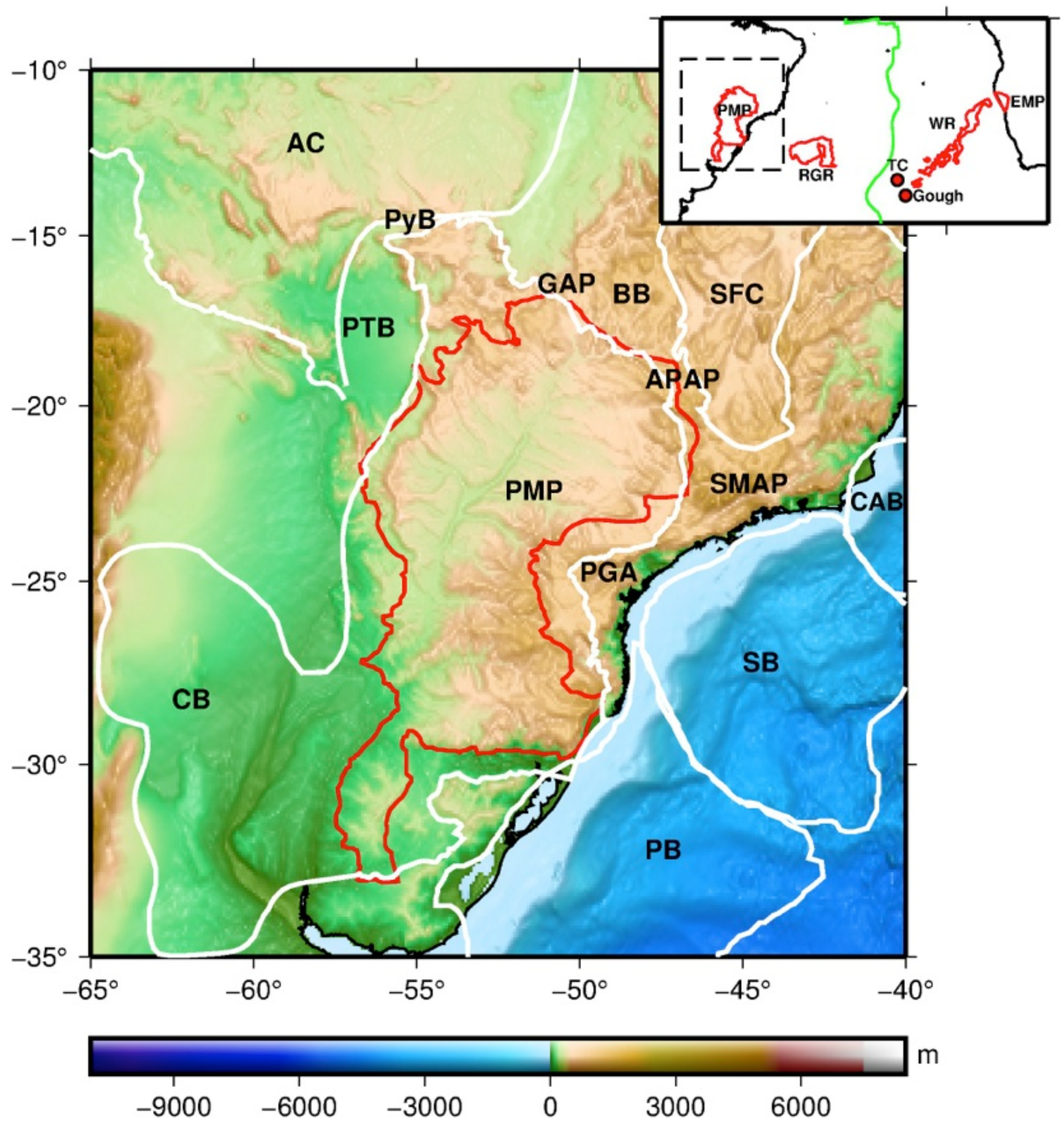

Figure 1. Topography and bathymetry map of the southeastern South America showing location of geological-tectonic provinces in the study area (black dashed square in the small map in the upper right). The study area encompasses the São Francisco craton (SFC), Amazonian craton (AC), Chaco-Paraná basin (CB), Pelotas basin (PB), Santos basin (SB), Campos basin (CAB), Pantanal basin (PTB), Paraguay belt (PyB), Brasília belt (BB), Alto Paranaíba Alkaline Province (APAP), Goiás Alkaline Province (GAP), Serra do Mar Alkaline Province (SMAP), Ponta Grossa Arch (PGA). The superposed map of the southern Atlantic region shows the locations of (red contour) the Paraná Magmatic Province (PMP), Rio Grande Rise (RGR), Walvis Ridge (WR), Etendeka Magmatic Province (EMP), (green line) the Mid-Atlantic Ridge and (red circles) the Tristan da Cunha (TC) and Gough hotspots

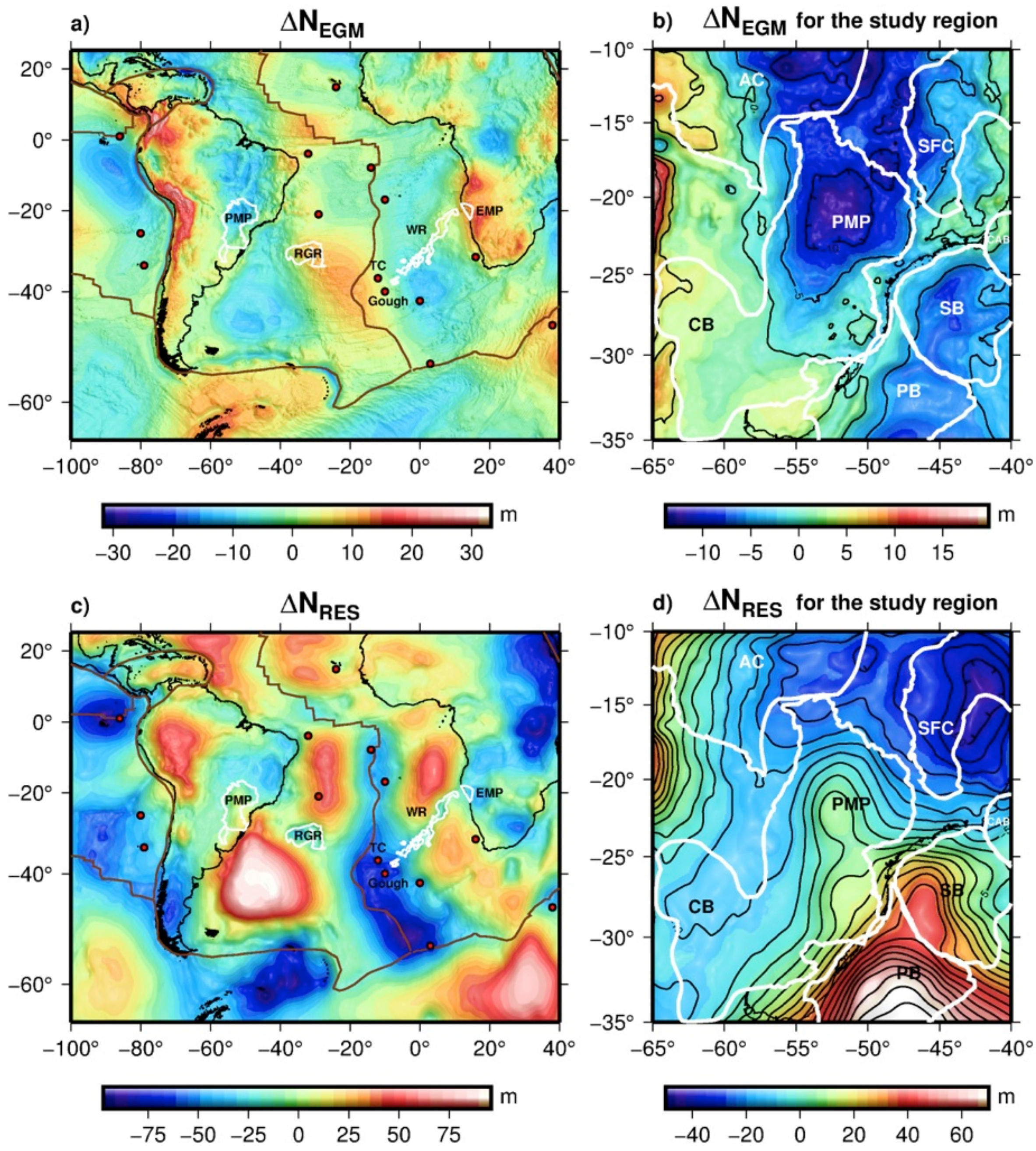

Figure 2. (a) Geoid height after removing the long-wavelength components (> 5400 km) by subtracting the EGM2008 [*Pavlis et al.*, 2012] of degree and order 7 from the EGM2008 up to degree and order 2159. (b) Geoid height for the study area. (c) Filtered residual geoid anomaly obtained after removing crustal effects from the geoid in Figure 2a. The wavelength spectrum of the residual geoid ranges between 111 and 5400 km. (d) Residual geoid anomaly map for the study area. White contours indicate the limits of tectonic provinces shown in Figure 1. Brown thick lines are plate boundaries. Red circles show hotspot locations.

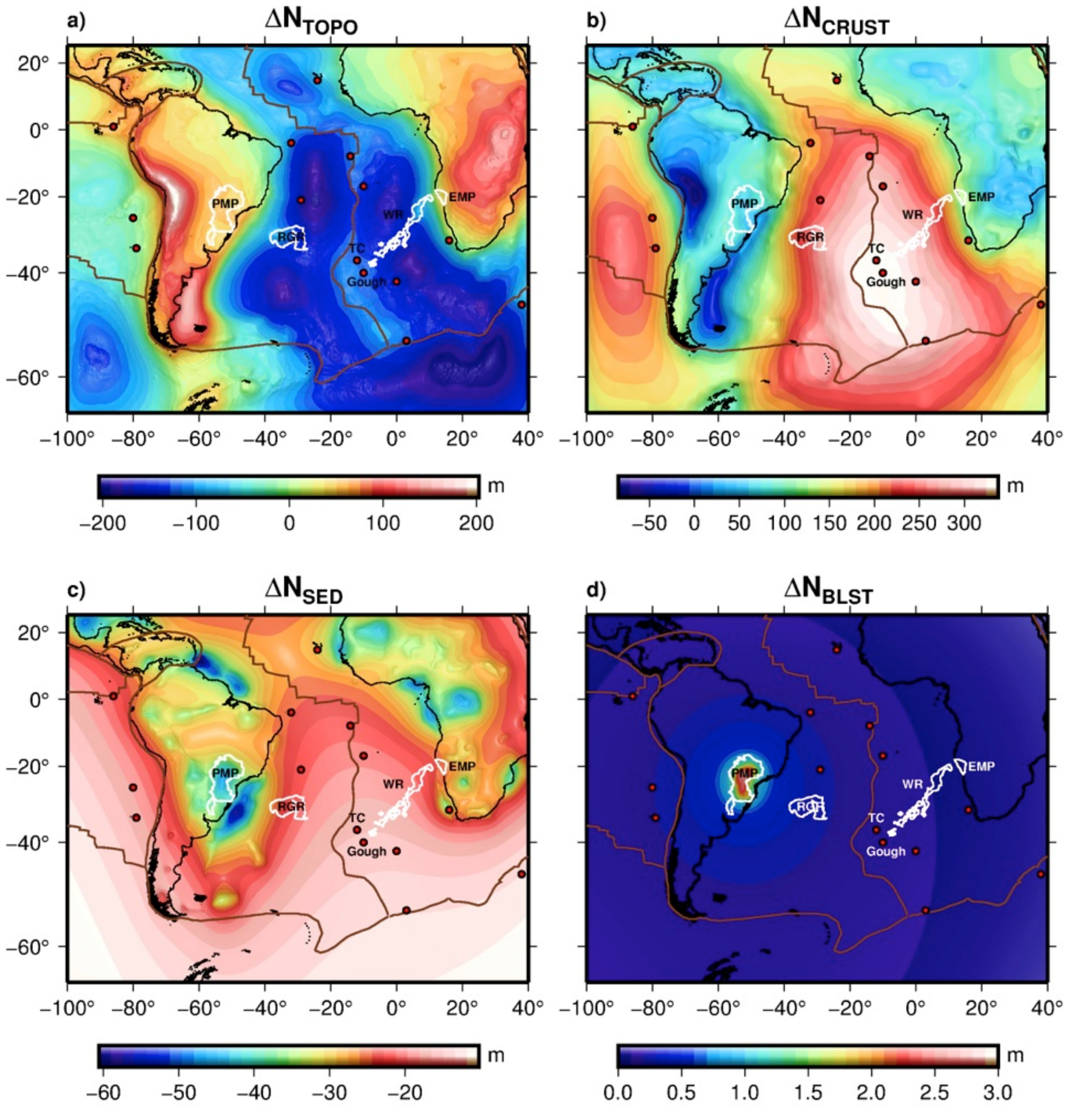

Figure 3. (a), (b), (c) and (d) are the geoid components due to topographic masses, Moho depth variations, sedimentary and basalt thickness, respectively. White contours indicate the limits of magmatic provinces shown in Figure 1. Brown lines are plate boundaries. Red circles show hotspot locations.

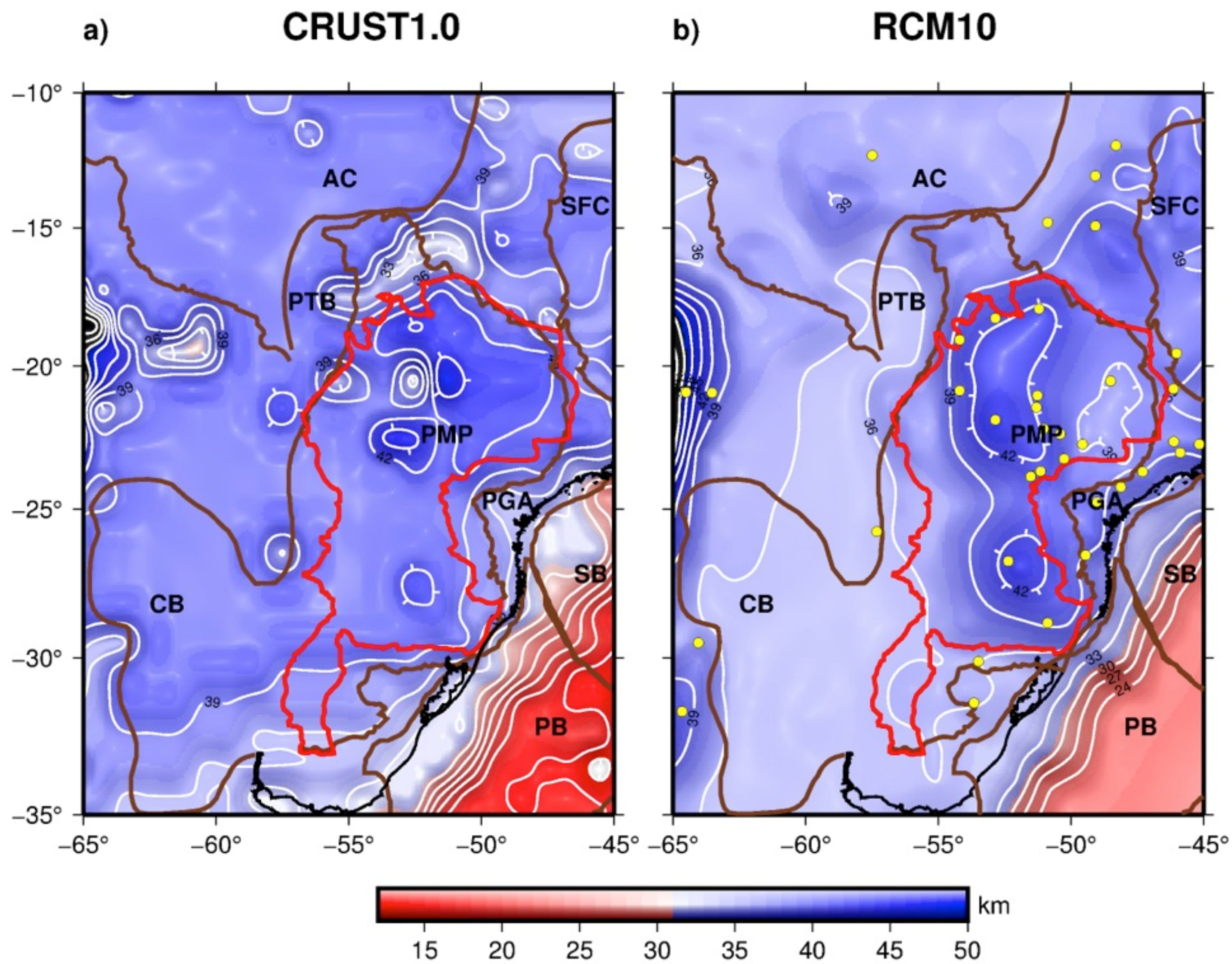

Figure 4. (a) Moho depth from CRUST1.0 (b) Moho depth using compilation of receiver function (RF) values of *Assumpção et al.* [2013] (yellow dots) and local isostatic modeling of observed topography. Brown contours indicate the limits of tectonic provinces shown in Figure 1. Red color represents the contour of the PMP.

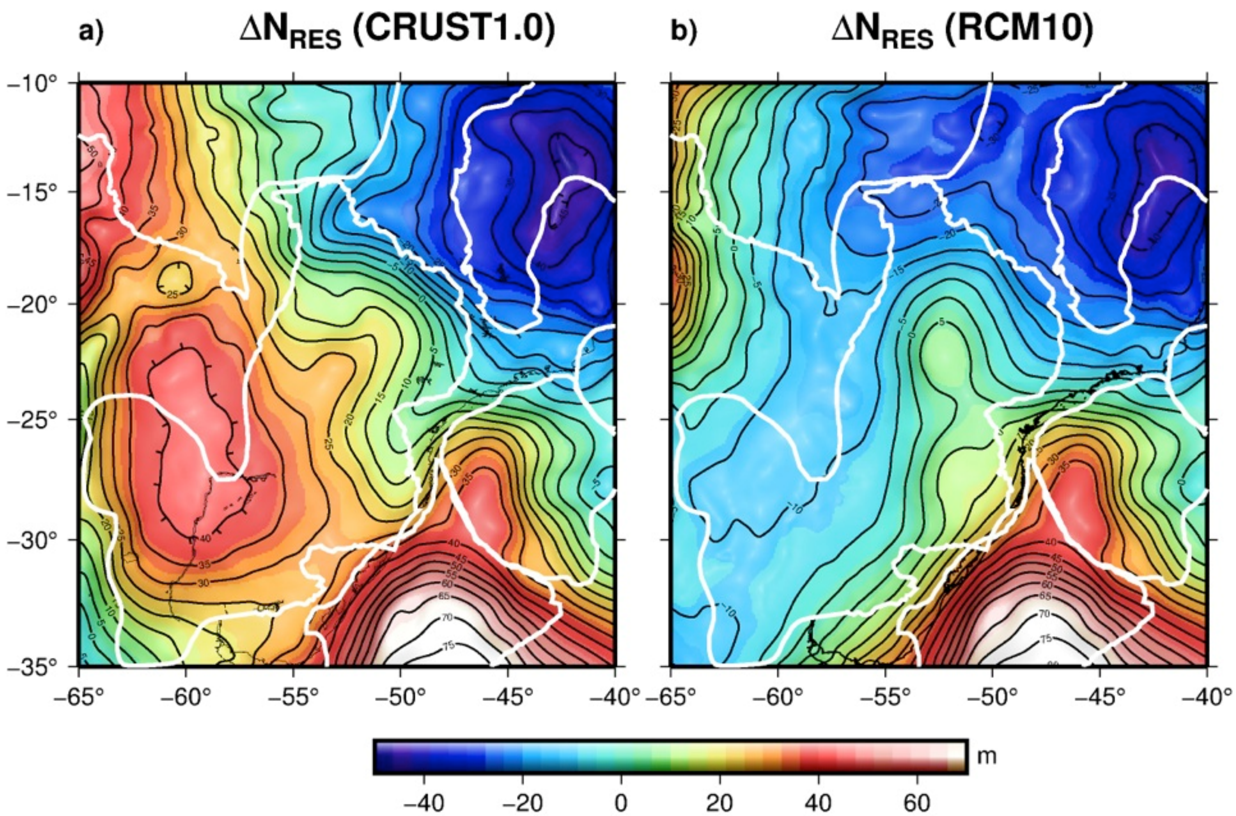

Figure 5. Residual geoid anomaly in the study area using (a) CRUST1.0 and (b) results from regional seismic studies and isostatic modeling. The residual geoid maps contains wavelengths between 111 and 5400 km.

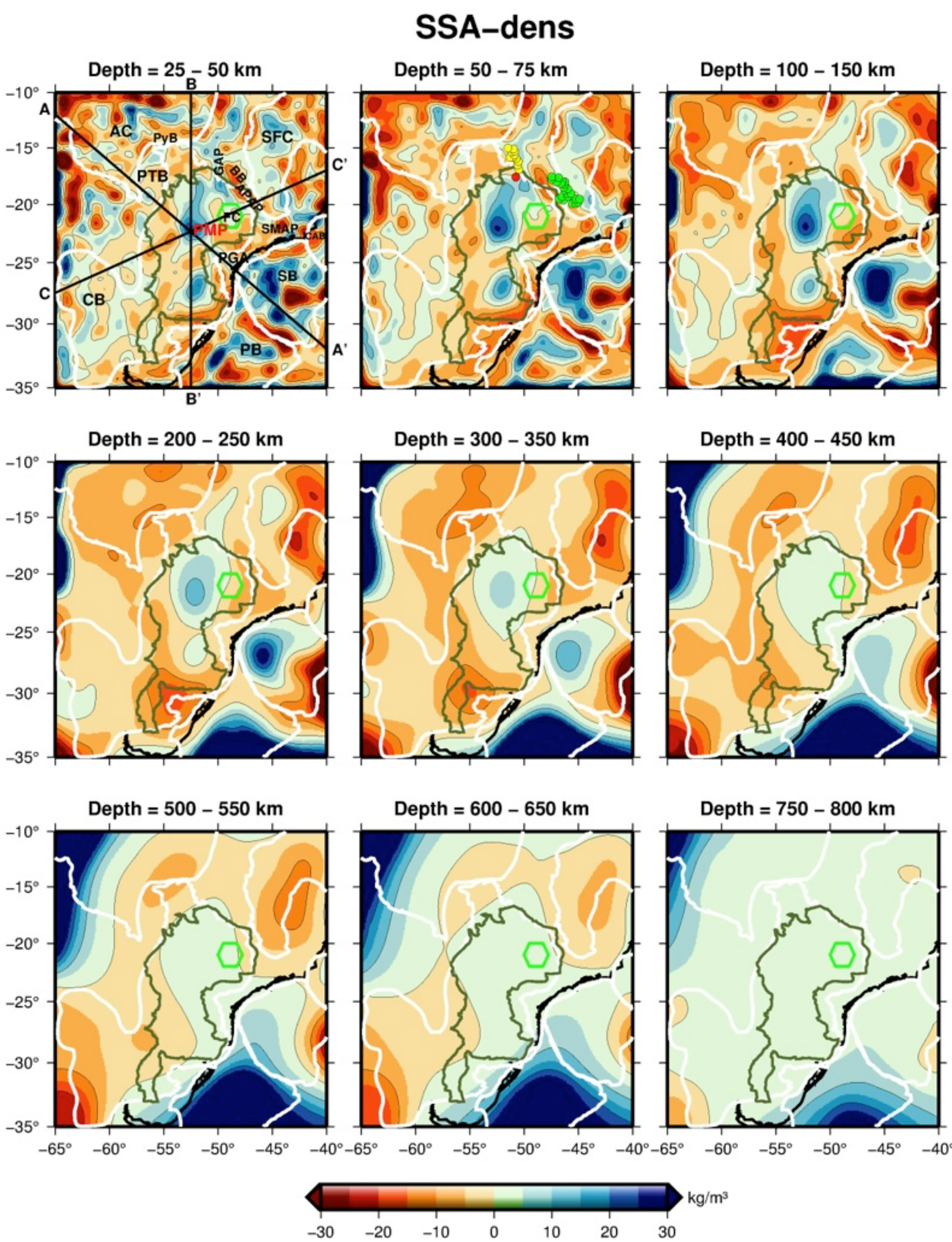

Figure 6. Slices of the estimated density model for the study area (SSA-dens) at different depths. A-A', B-B' and C-C' are profiles from where vertical cross-sections were extracted (see Figure 7a). FC: Fossil conduit (green hexagon) mapped by *VanDecar et al.* [1995]. White thick lines are the contours of tectonic provinces. For full name of tectonic and igneous provinces, (abbreviation in the first slice) see caption in Figure 1. Green line is the limit of the PMP. Yellow and green circles are the locations of the alkaline intrusions of the GAP and APAP, respectively. Red circle are the xenolith samples studied by *Carlson et al.* [2007].

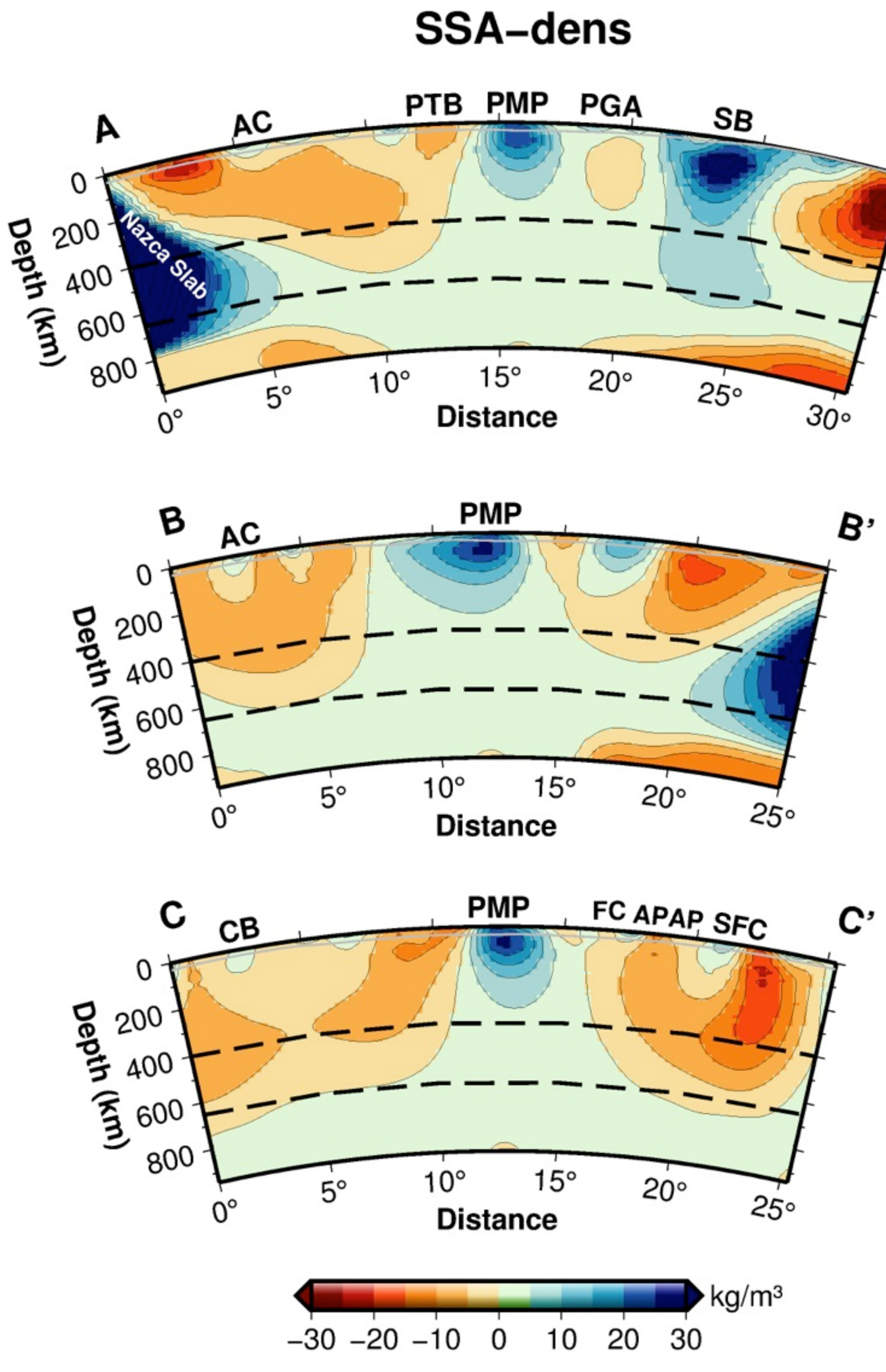

Figure 7. Vertical cross sections of SSA-dens along the A-A', B-B' and C-C' profiles. Gray line is the Moho depth and black dashed lines are the depth of 410 and 660 km discontinuities. PTB: Pantanal Basin; AC: Amazonian craton; SFC: São Francisco craton; PyB: Paraguay belt; BB: Brasília Belt; APAP: Alto Paranaíba Alkaline Province; SB: Santos basin; PGA: Ponta Grossa Arch; PMP: Paraná Magmatic Province. FC: Fossil conduit mapped by *VanDecar et al.* [1995].

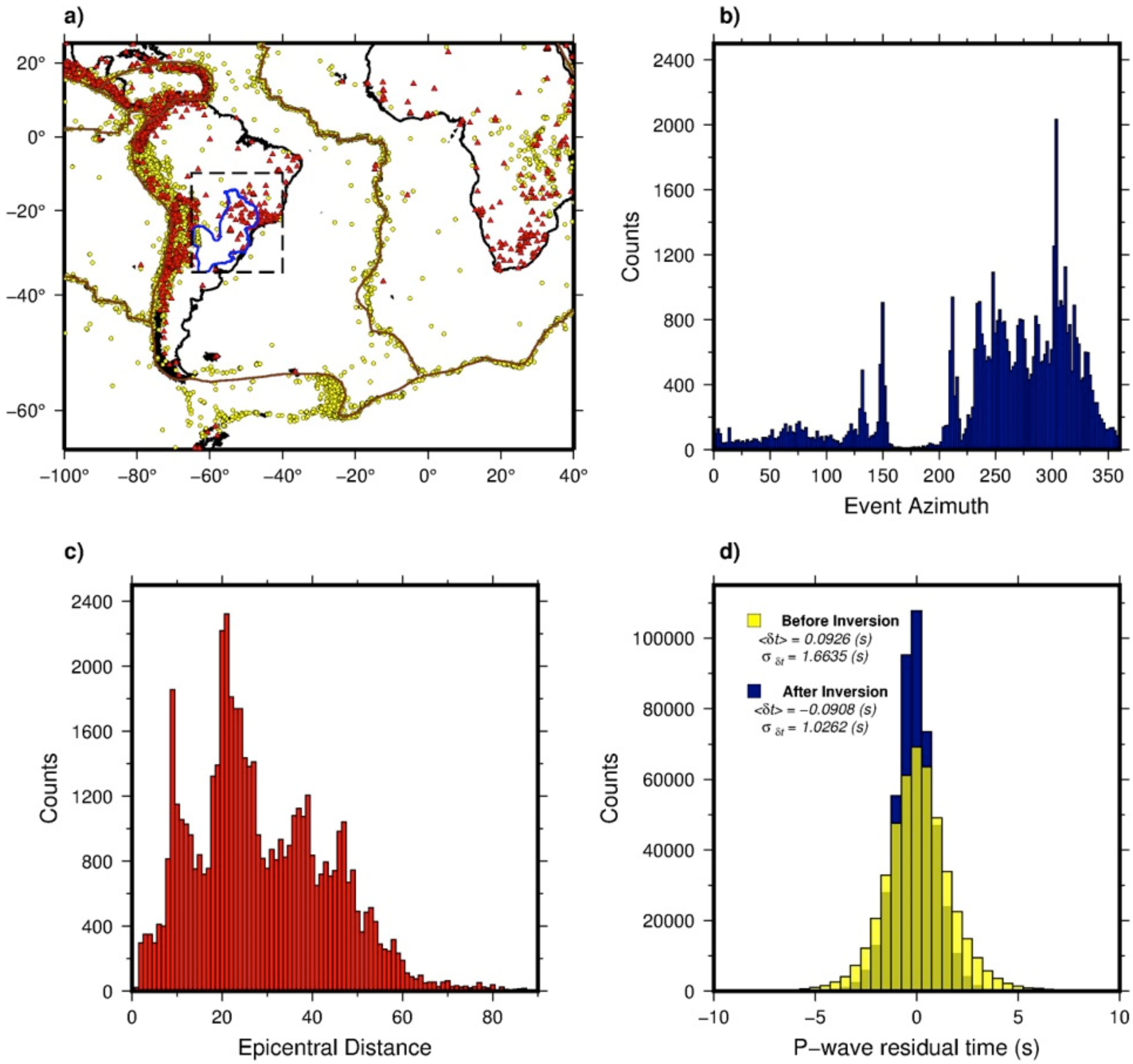

Figure 8. (a) Location of sources and receivers used in the P-wave tomography. Yellow dots are the epicenters of the selected events. Red triangles are the seismic stations. (b) Histogram showing the azimuthal distribution of events recorded by stations within the study area (black dashed square). Histogram showing the epicentral distance distribution of events recorded by the seismic stations within the study area. (d) Histogram for the P-wave travel-time residuals before the inversion (yellow bins) and after the inversion (blue bins).

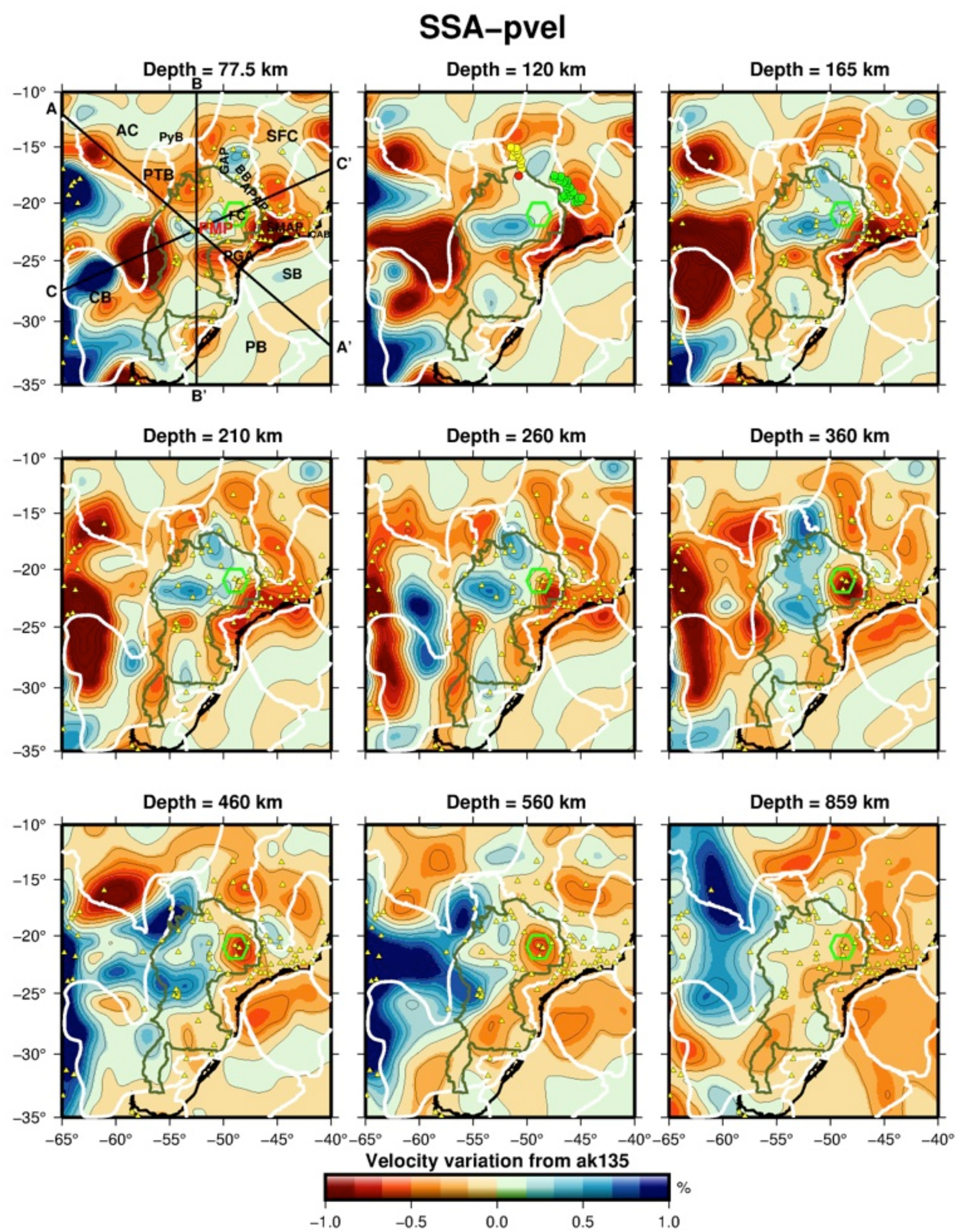

Figure 9. Slices of the estimated velocity model (SSA-pvel) at different depths from the inversion of the P-wave delay travel-times (Figure 8b). A-A', B-B' and C-C' are profiles where vertical cross sections were extracted (see Figure 10). FC: Fossil conduit (green hexagon) mapped by *VanDecar et al.* [1995]. White thick lines are the contours of tectonic provinces. For full name of tectonic and igneous provinces (abbreviation in the first slice) see caption in Figure 1. Green line is the limit of the PMP. Yellow triangles are the seismic stations. Yellow and green circles are the alkaline intrusions of the GAP and APAP. Red circles are the xenolith samples studied by *Carlson et al.* [2007].

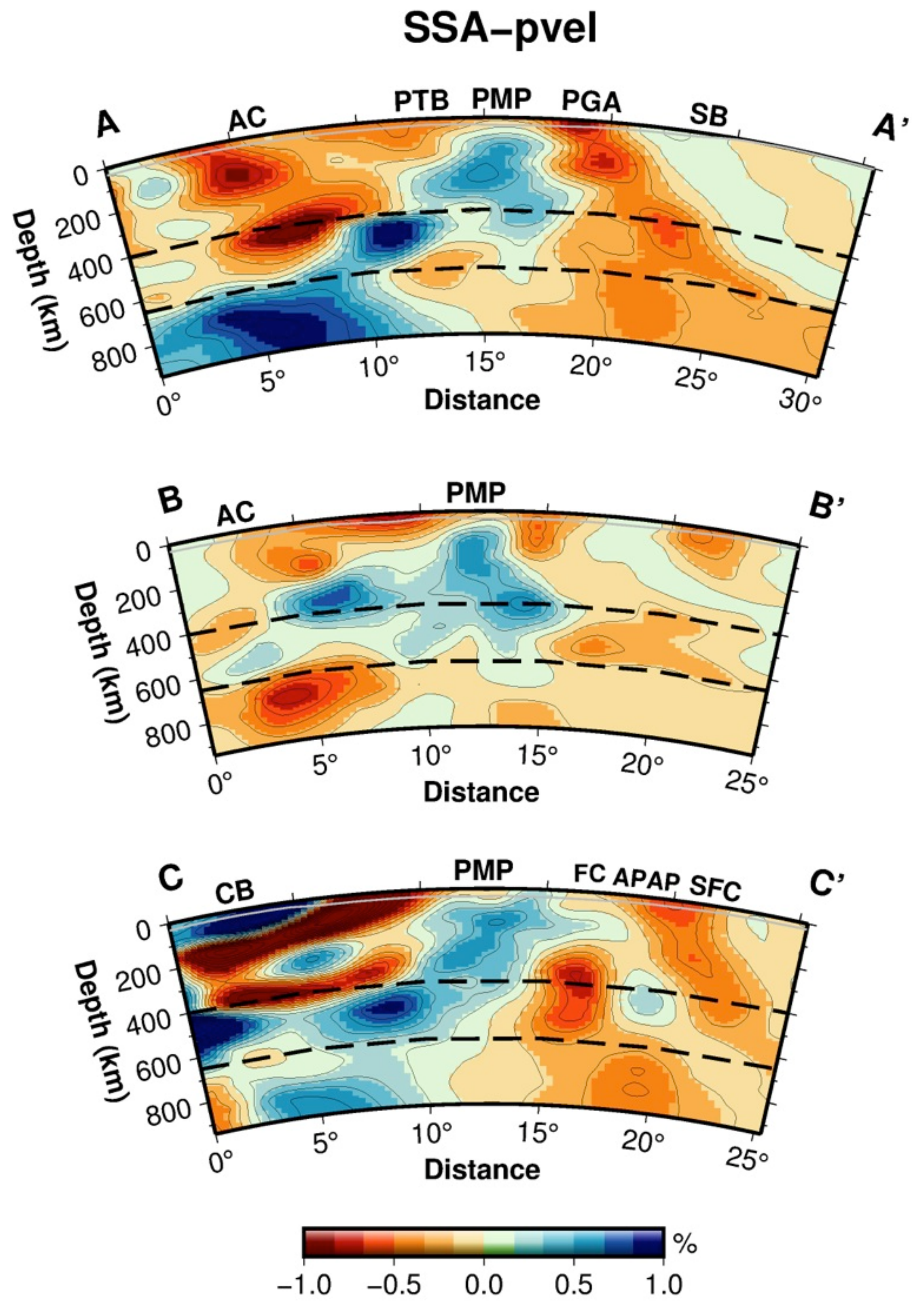

Figure 10. Vertical cross sections of SSA-pvel along the A-A', B-B' and C-C' profiles. Black dashed lines are the depth of 410 and 660 km discontinuities. PTB: Pantanal basin; AC: Amazon craton; SFC: São Francisco craton; PyB: Paraguay belt; BB: Brasília belt; APAP: Alto Paranaíba Alkaline Province; SB: Santos basin; PGA: Ponta Grossa Arch; PMP: Paraná Magmatic Province. FC: Fossil conduit mapped by *VanDecar et al.* [1995].

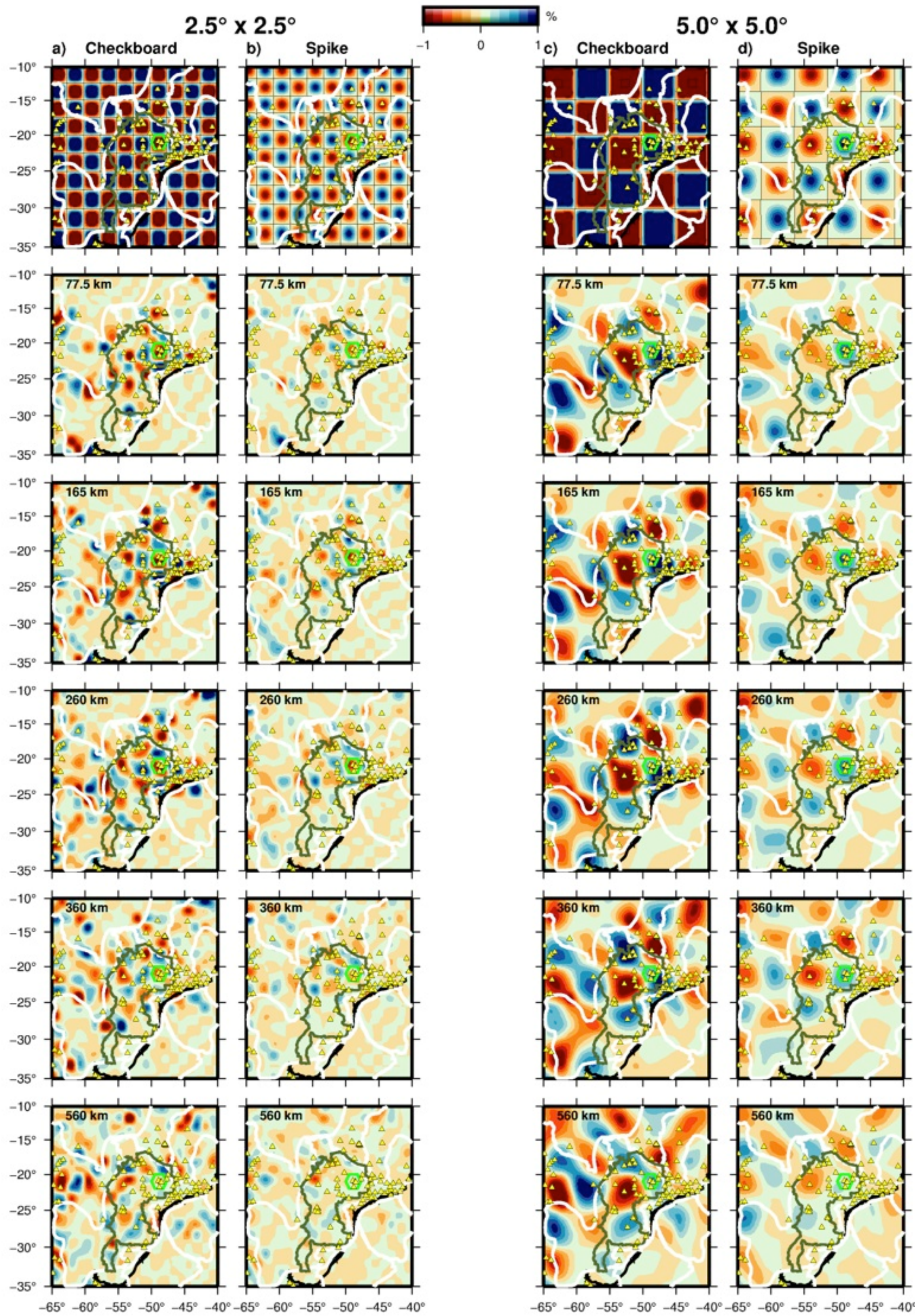

Figure 11. Slices of the recovered velocity model for a) and c) the checkboard and b) and d) spike test at different depths using perturbed cell sizes of 2.5˚×2.5˚ and of 5˚×5˚. White lines are the contours of tectonic provinces as shown in Figure 1. Green line is the limit of the PMP. Green hexagon is the location of the low-velocity fossil conduit mapped by *VanDecar et al.* [1995]. Yellow triangles are the seismic stations in the study area.

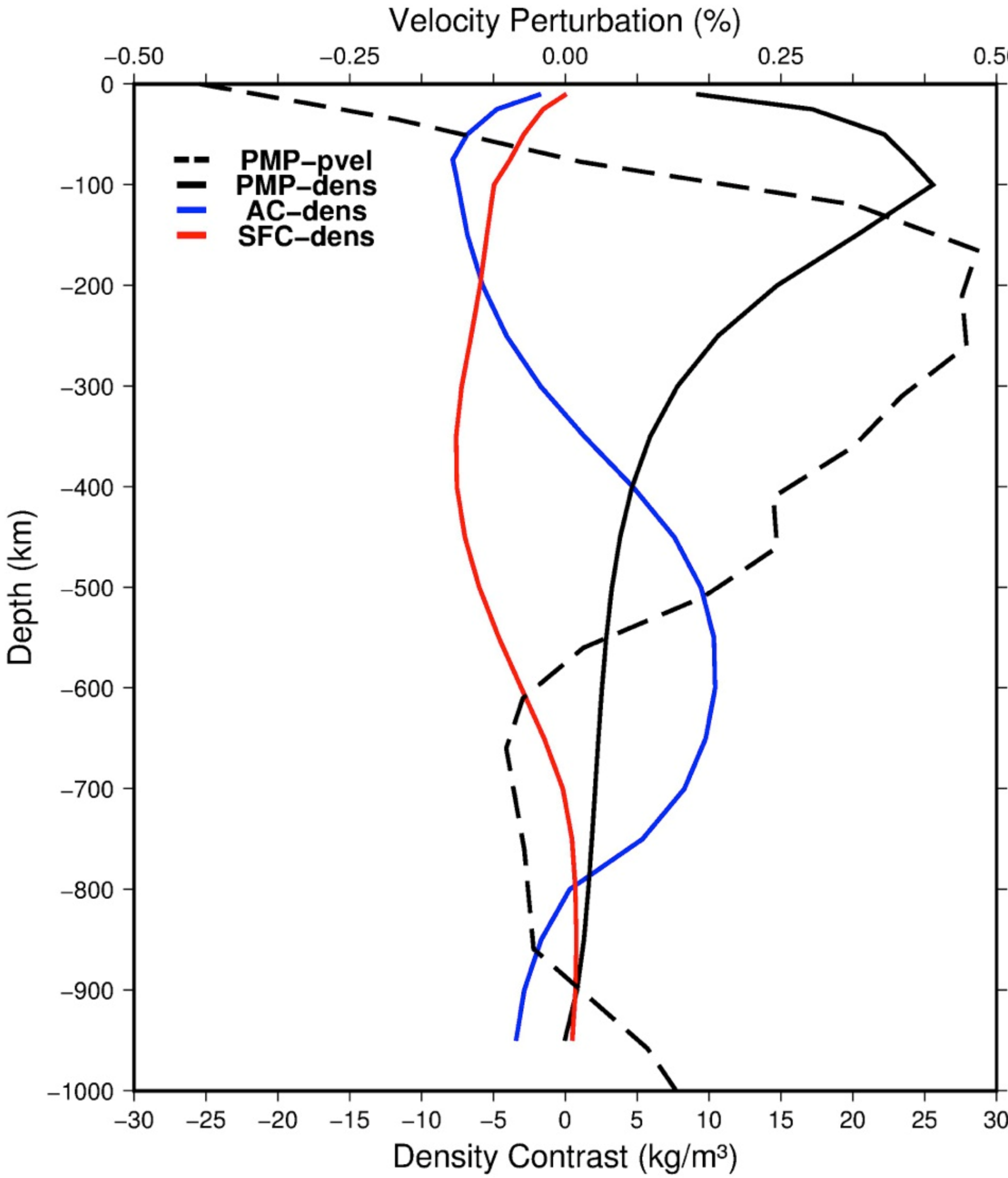

Figure 12. Averaged density perturbation as a function of depth from SSA-dens (Figure 6) beneath the SFC and AC, PMP. Black dashed curve is the averaged velocity perturbation from SSA-pvel (Figure 9) beneath the PMP.

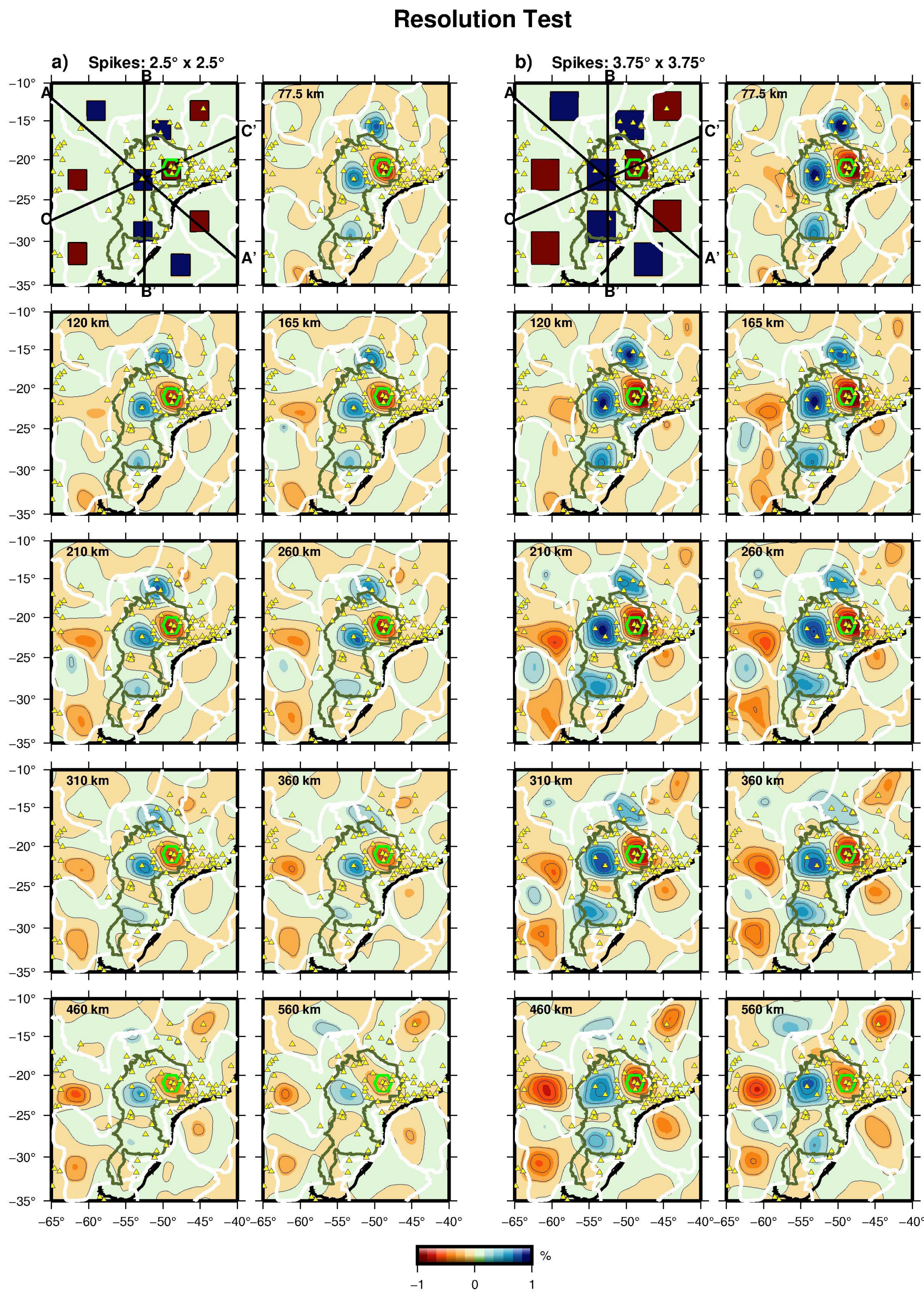

Figure S1. Slices of the recovered velocity model for spike tests at different depths using perturbed sparse cell sizes of 2.5˚×2.5˚ and of 3.75˚×3.75˚. White lines are the contours of tectonic provinces as shown in Figure 1. Green line is the limit of the PMP. Green hexagon is the location of the low-velocity fossil conduit mapped by *VanDecar et al.* [1995]. Yellow triangles are the seismic stations in the study area.

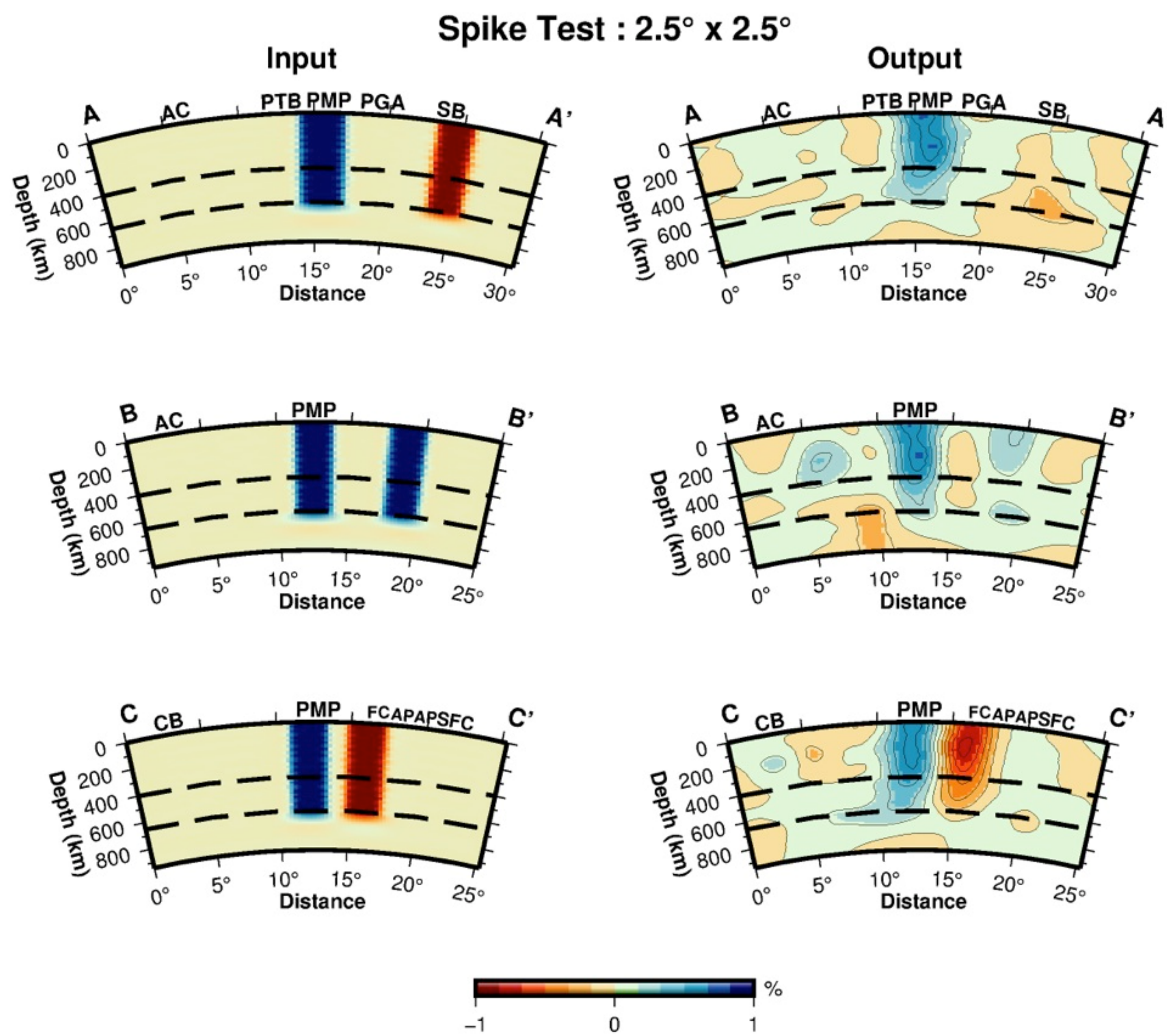

Figure S2. Vertical cross sections of the recovered velocity model for sparse spikes of cell sizes of 2.5˚×2.5˚ along the A-A’, B-B’ and C-C’ profiles (see Figure S1). Black dashed lines are the depth of 410 and 660 km discontinuities. PTB: Pantanal basin; AC: Amazon craton; SFC: São Francisco craton; PyB: Paraguay belt; BB: Brasília belt; APAP: Alto Paranaíba Alkaline Province; SB: Santos basin; PGA: Ponta Grossa Arch; PMP: Paraná Magmatic Province. FC: Fossil conduit mapped by *VanDecar et al.* [1995].

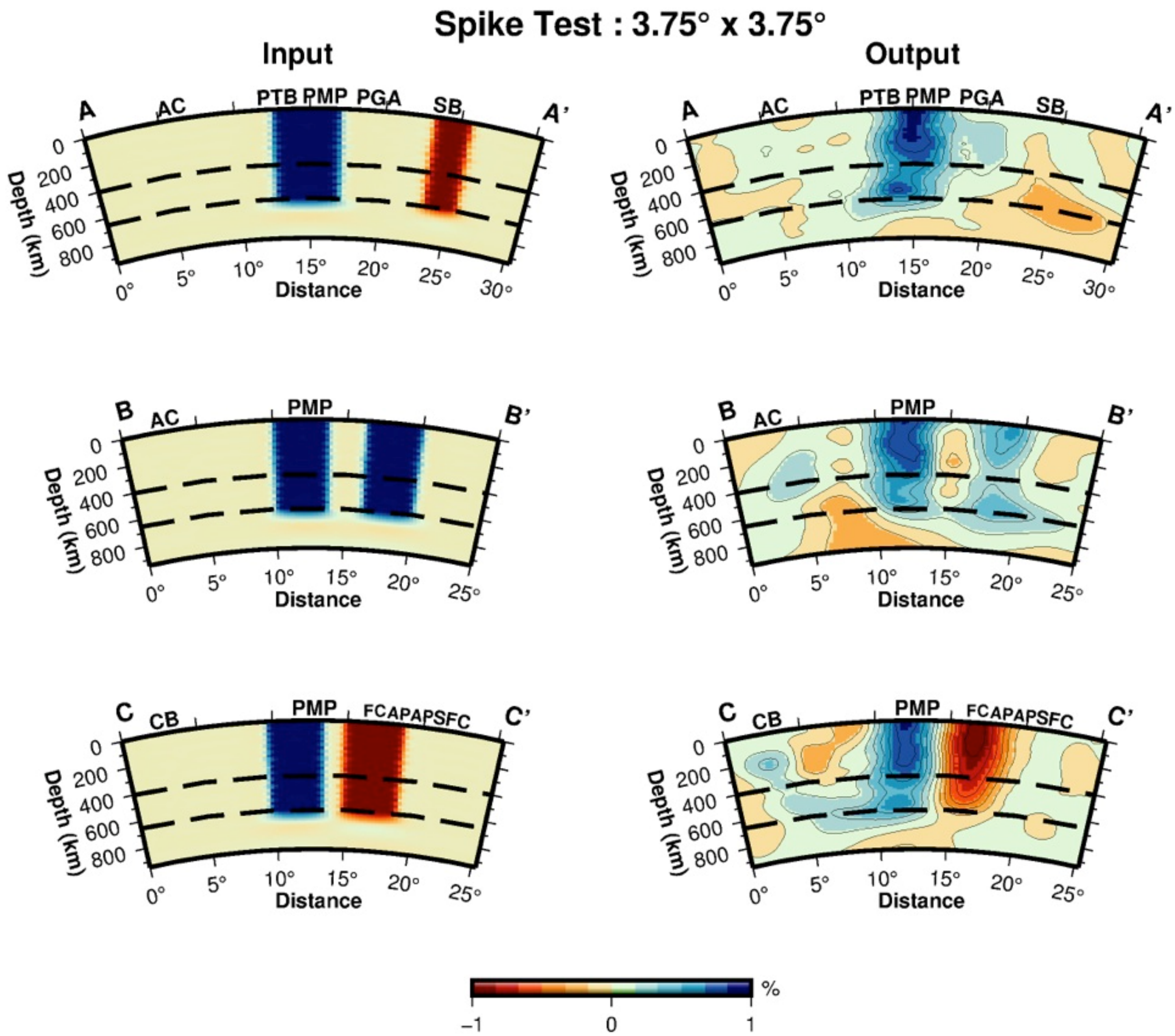

Figure S3. Vertical cross sections of the recovered velocity model for sparse spikes of cell sizes of 3.75˚×3.75˚ along the A-A', B-B' and C-C' profiles (see Figure S1). Black dashed lines are the depth of 410 and 660 km discontinuities. PTB: Pantanal basin; AC: Amazon craton; SFC: São Francisco craton; PyB: Paraguay belt; BB: Brasília belt; APAP: Alto Paranaíba Alkaline Province; SB: Santos basin; PGA: Ponta Grossa Arch; PMP: Paraná Magmatic Province. FC: Fossil conduit mapped by *VanDecar et al.* [1995].

Figure 1. Figure

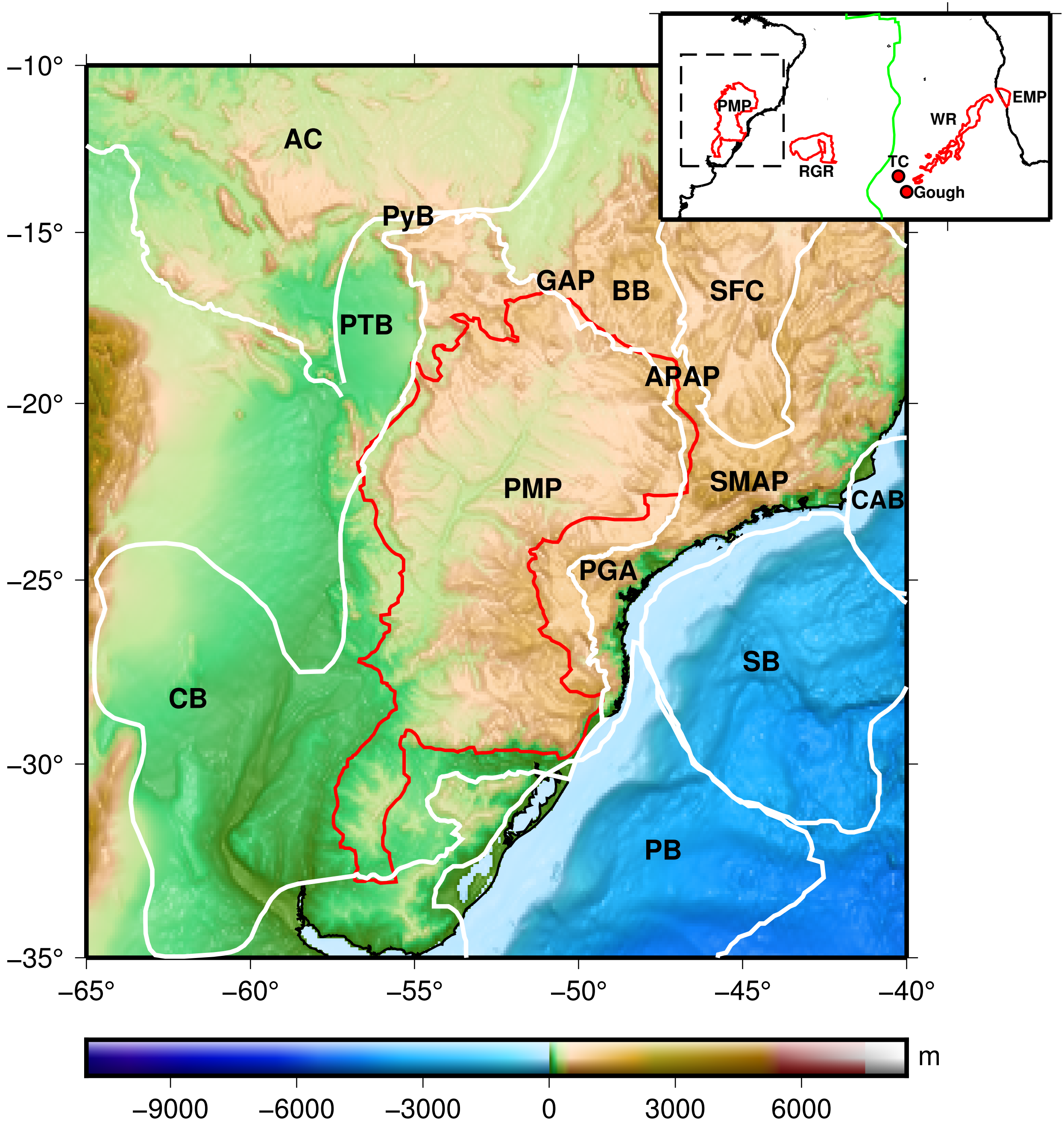
AC
PyB
PTB
GAP
BB
SFC
APAP
PMP
SMAP
CAB
PGA
SB
CB
PB
PMP
RGR
TC
Gough
WR
EMP
−10°
−15°
−20°
−25°
−30°
−35°
−65°
−60°
−55°
−50°
−45°
−40°
−9000
−6000
−3000
0
3000
6000
m

Figure 2. Figure

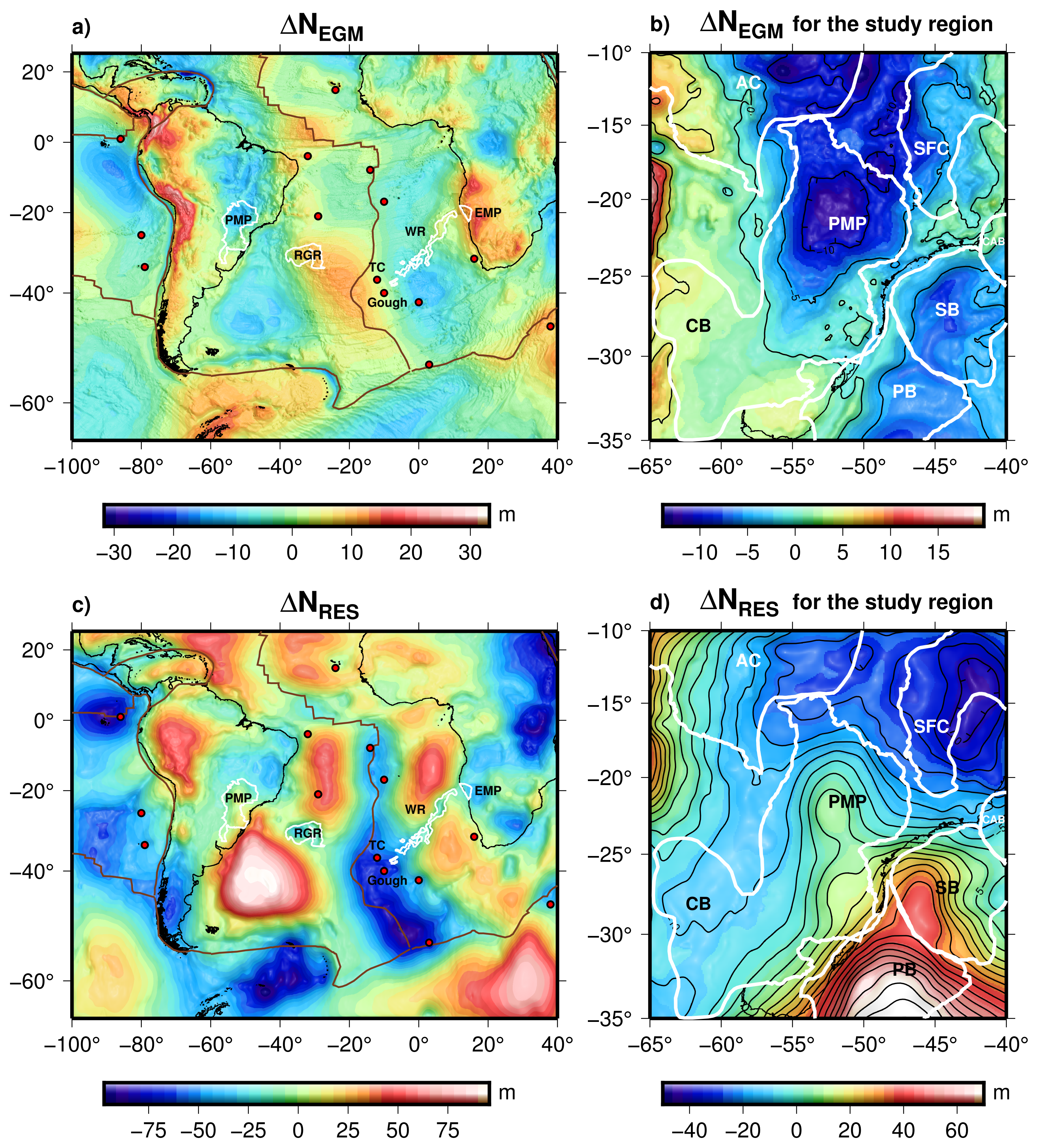

a)
ΔN_EGM
b)
ΔN_EGM for the study region
c)
ΔN_RES
d)
ΔN_RES for the study region
PMP
RGR
WR
EMP
TC
Gough
AC
SFC
CAB
SB
CB
PB
m

Figure 3. Figure

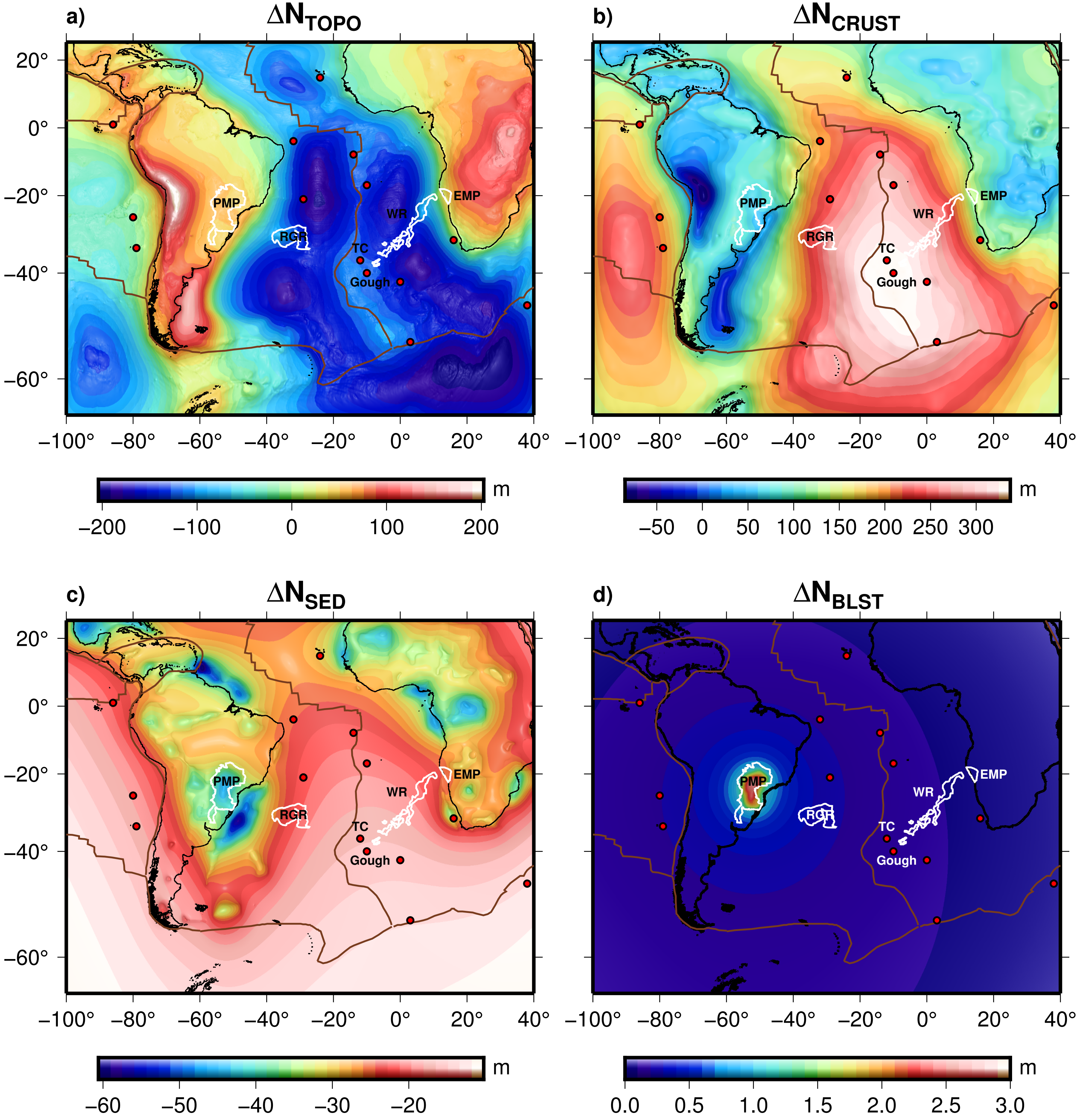

a)
ΔN_{TOPO}
b)
ΔN_{CRUST}
c)
ΔN_{SED}
d)
ΔN_{BLST}
PMP
RGR
WR
EMP
TC
Gough
20°
0°
−20°
−40°
−60°
−100°
−80°
−60°
−40°
−20°
0°
20°
40°
m
−200
−100
0
100
200
−50
0
50
100
150
200
250
300
−60
−50
−40
−30
−20
0.0
0.5
1.0
1.5
2.0
2.5
3.0

Figure 4. Figure

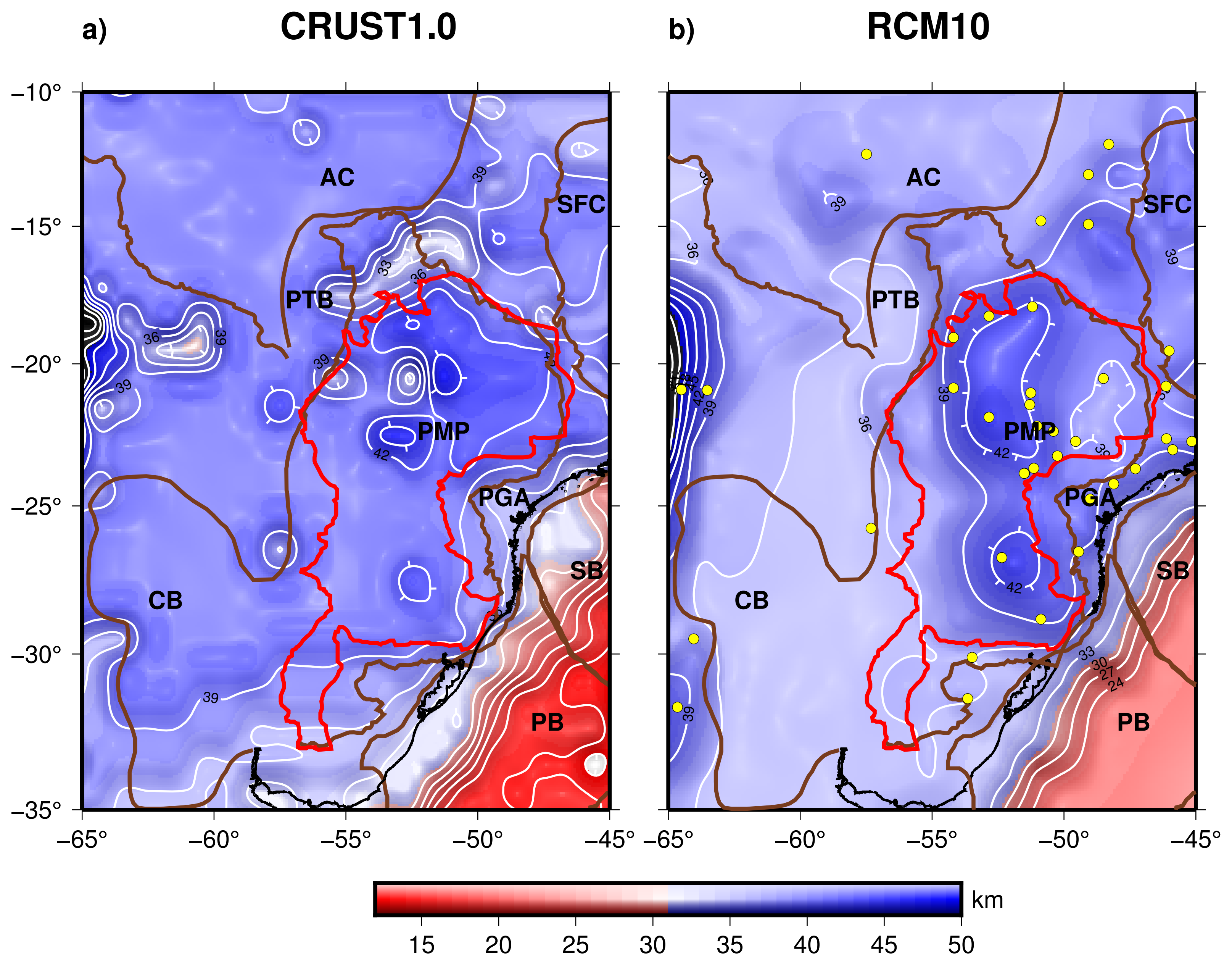

a)
CRUST1.0
b)
RCM10
AC
SFC
PTB
PMP
PGA
CB
SB
PB
−10°
−15°
−20°
−25°
−30°
−35°
-65°
-60°
-55°
-50°
-45°
km
15
20
25
30
35
40
45
50

Figure 5. Figure

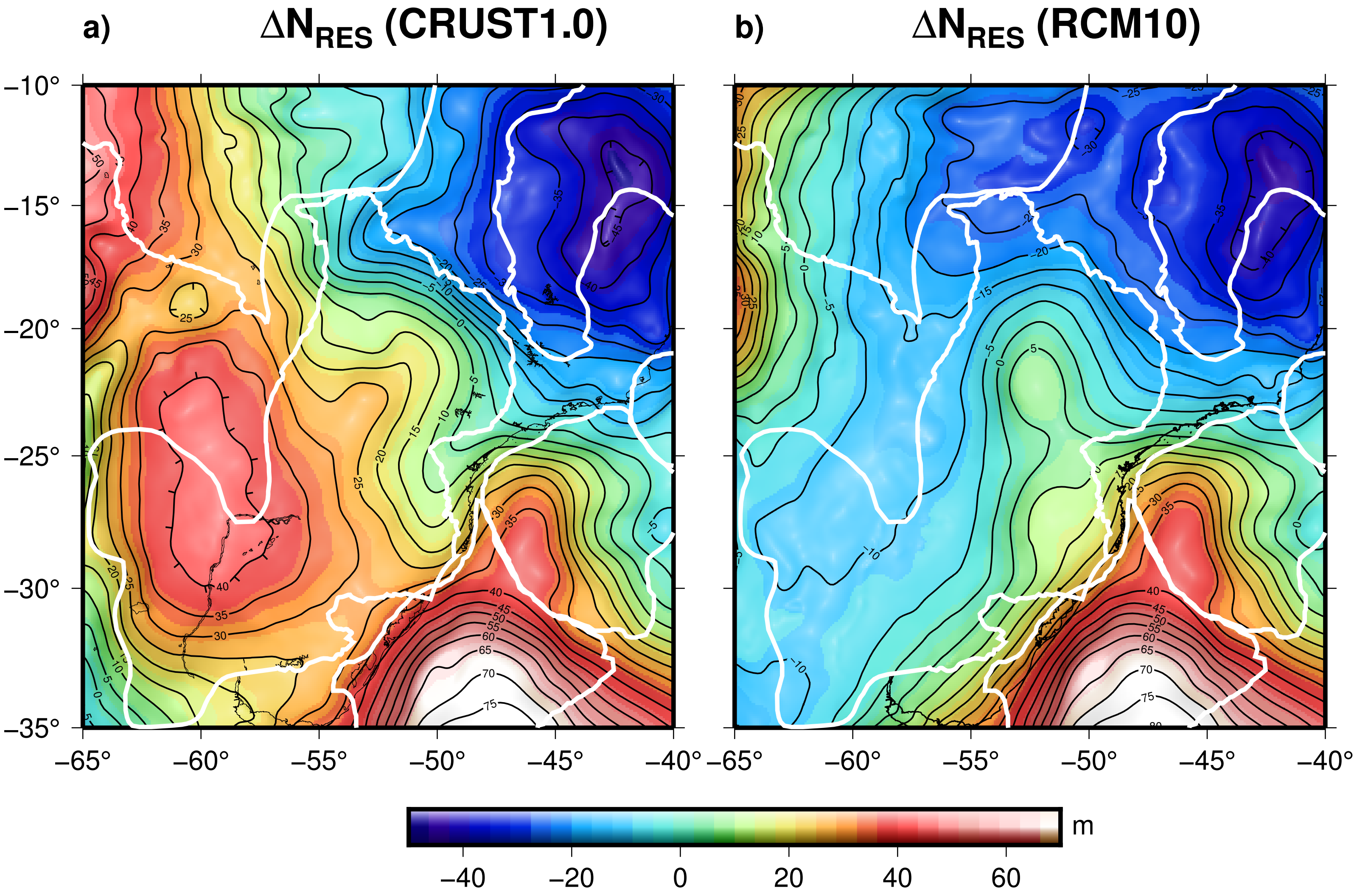

a)
ΔN_RES (CRUST1.0)
b)
ΔN_RES (RCM10)
−10°
−15°
−20°
−25°
−30°
−35°
−65°
−60°
−55°
−50°
−45°
−40°
m
−40
−20
0
20
40
60

Figure 6. Figure

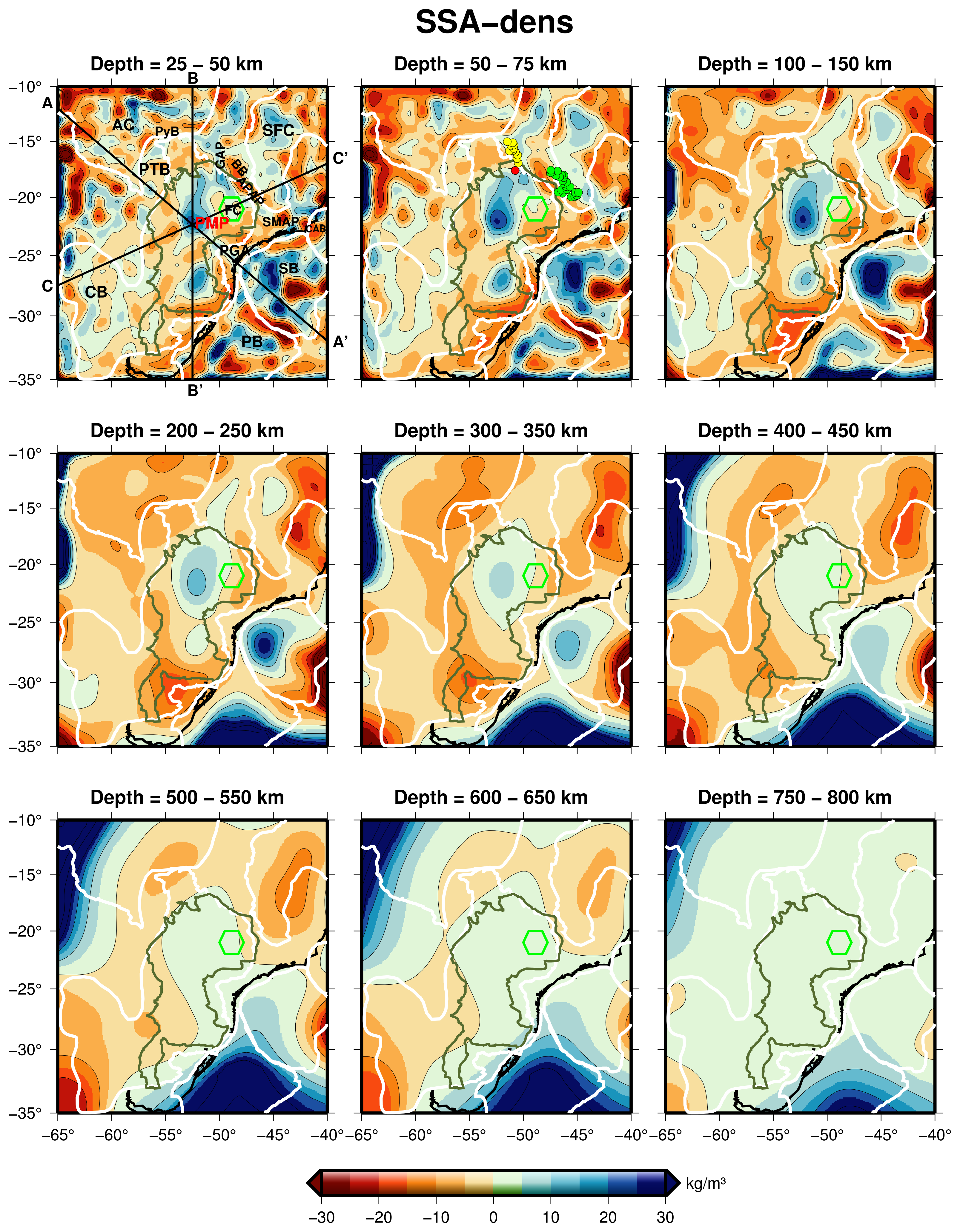
SSA−dens
Depth = 25 − 50 km
Depth = 50 − 75 km
Depth = 100 − 150 km
Depth = 200 − 250 km
Depth = 300 − 350 km
Depth = 400 − 450 km
Depth = 500 − 550 km
Depth = 600 − 650 km
Depth = 750 − 800 km
A
A’
B
B’
C
C’
AC
PyB
SFC
PTB
GAP
BB
APIP
FC
PMP
SMAP
CAB
PGA
SB
CB
PB
−10°
−15°
−20°
−25°
−30°
−35°
−65°
−60°
−55°
−50°
−45°
−40°
−30
−20
−10
0
10
20
30
kg/m³

Figure 7. Figure

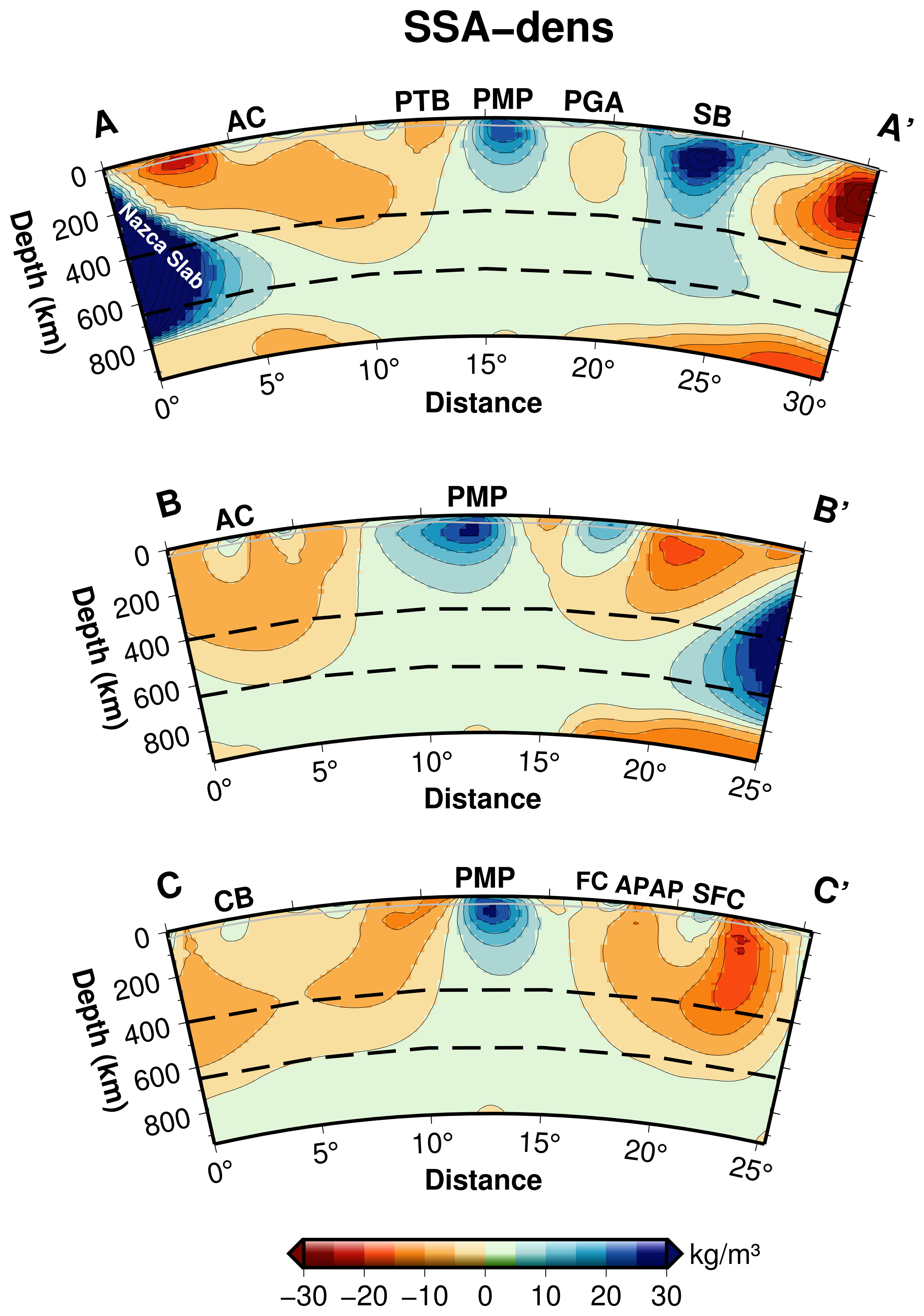
SSA–dens
A
AC
PTB
PMP
PGA
SB
A'
Nazca Slab
Depth (km)
0
200
400
600
800
0°
5°
10°
15°
20°
25°
30°
Distance
B
AC
PMP
B'
C
CB
PMP
FC
APAP
SFC
C'
kg/m3
−30
−20
−10
0
10
20
30

Figure 8. Figure

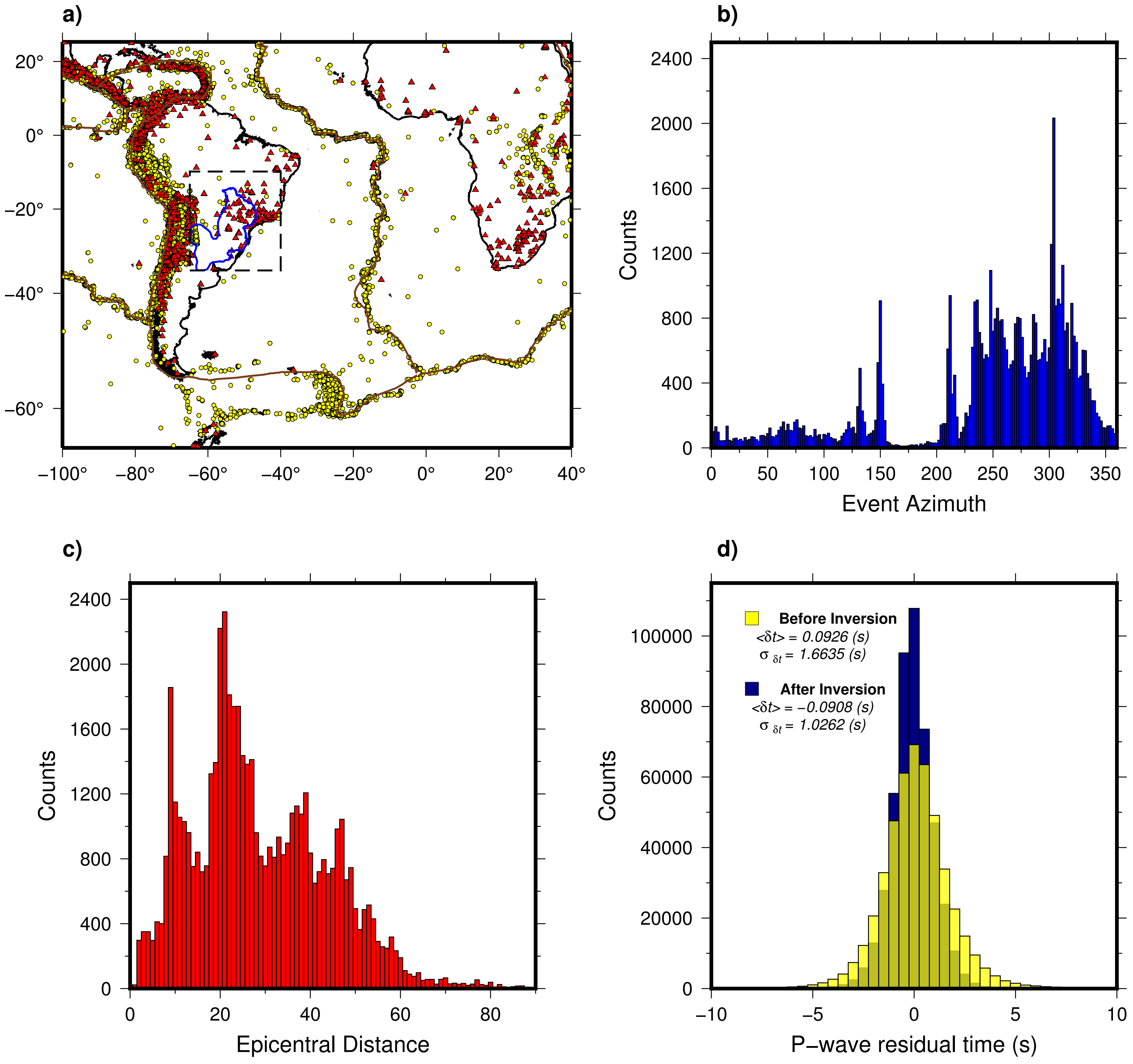

a)
20°
0°
−20°
−40°
−60°
−100°
−80°
−60°
−40°
−20°
0°
20°
40°
b)
Counts
Event Azimuth
0
400
800
1200
1600
2000
2400
0
50
100
150
200
250
300
350
c)
Counts
Epicentral Distance
0
400
800
1200
1600
2000
2400
0
20
40
60
80
d)
Before Inversion
<δt> = 0.0926 (s)
σ δt = 1.6635 (s)
After Inversion
<δt> = −0.0908 (s)
σ δt = 1.0262 (s)
Counts
P−wave residual time (s)
0
20000
40000
60000
80000
100000
−10
−5
0
5
10

Figure 9. Figure

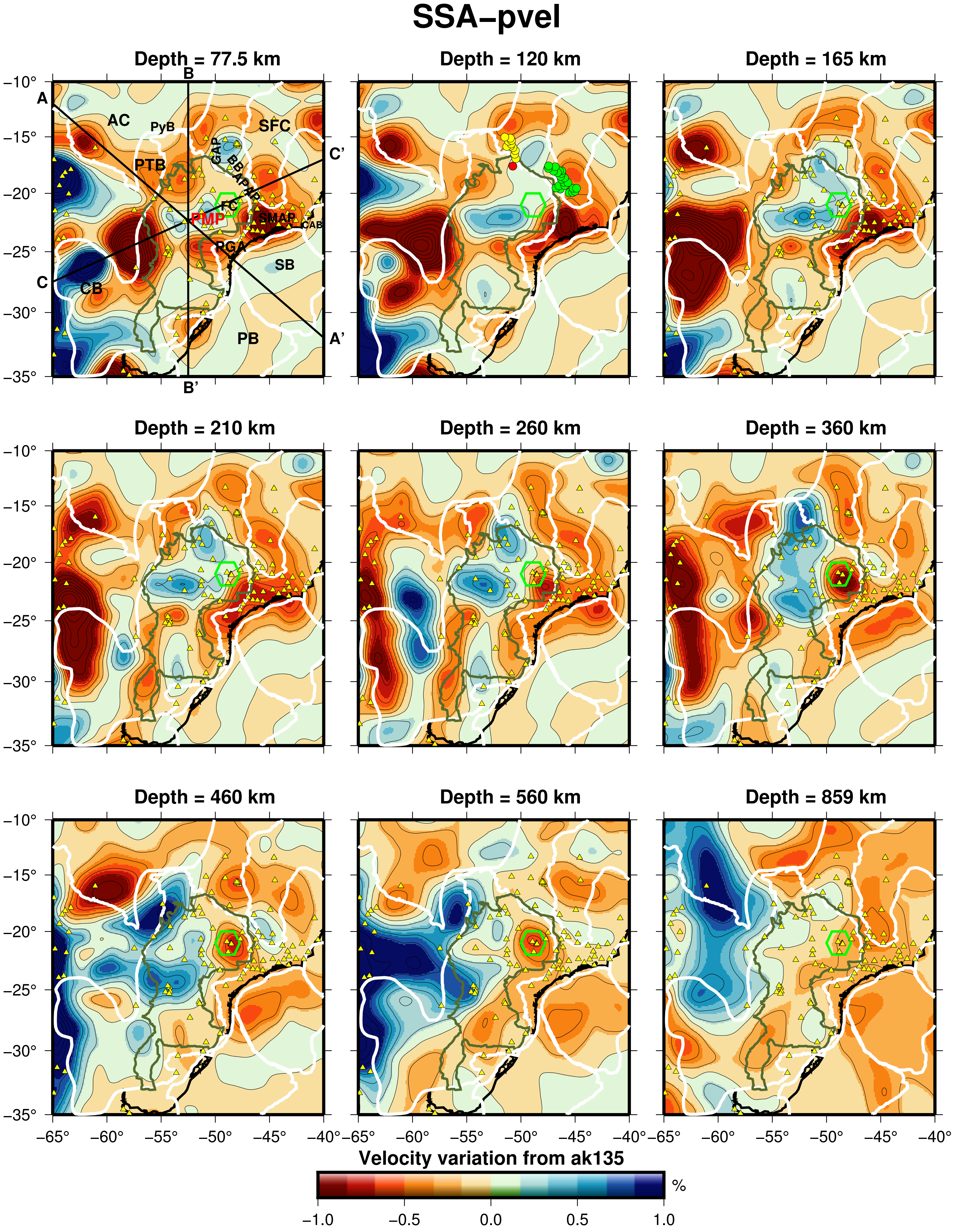

SSA−pvel
Depth = 77.5 km
Depth = 120 km
Depth = 165 km
Depth = 210 km
Depth = 260 km
Depth = 360 km
Depth = 460 km
Depth = 560 km
Depth = 859 km
A
A'
B
B'
C
C'
AC
PyB
SFC
GAP
BB
APAP
PTB
FC
PMP
SMAP
CAB
PGA
SB
CB
PB
−10°
−15°
−20°
−25°
−30°
−35°
−65°
−60°
−55°
−50°
−45°
−40°
Velocity variation from ak135
%
−1.0
−0.5
0.0
0.5
1.0

Figure 10. Figure

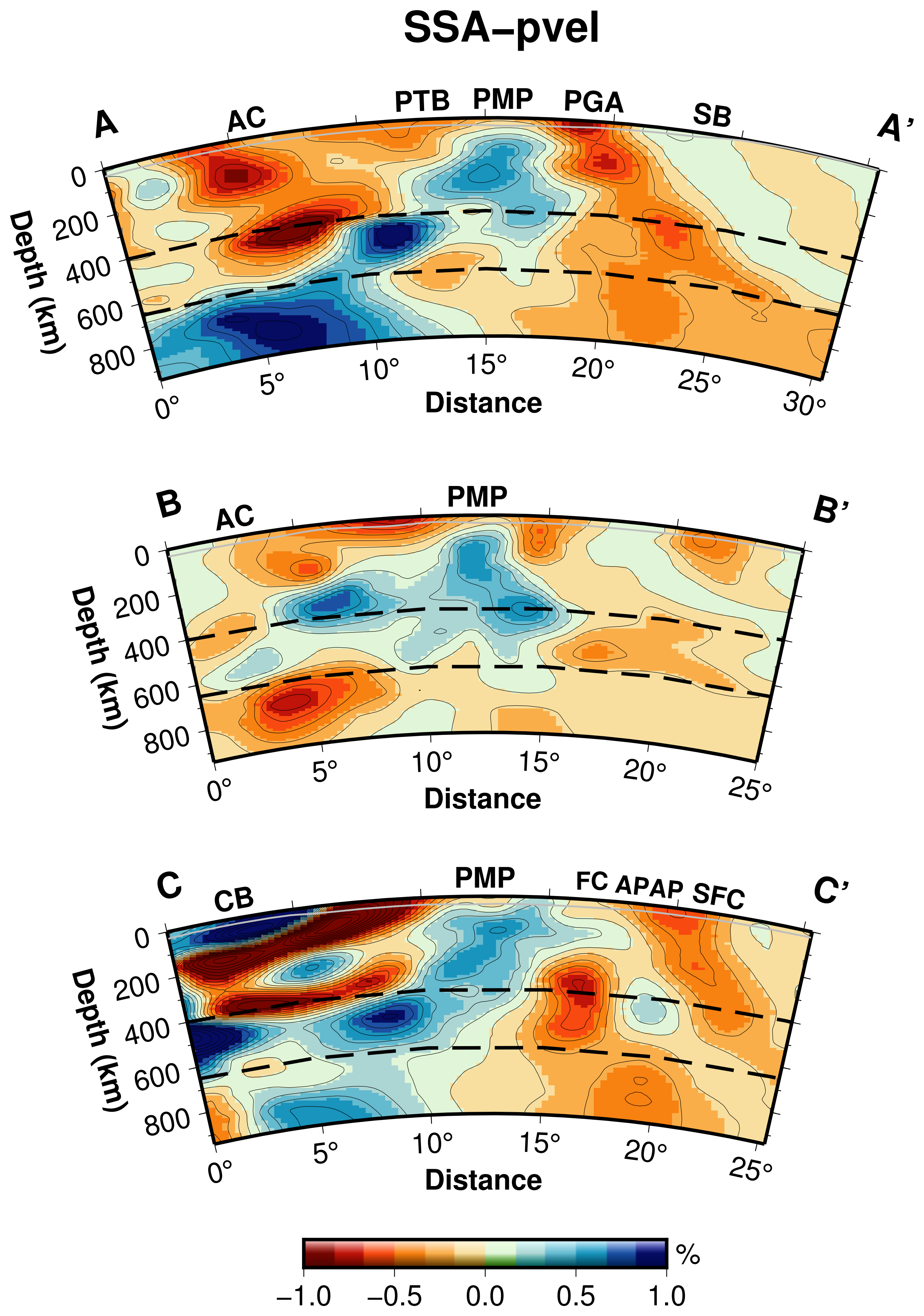
SSA–pvel
A
A'
AC
PTB
PMP
PGA
SB
Depth (km)
0
200
400
600
800
0°
5°
10°
15°
20°
25°
30°
Distance
B
B'
AC
PMP
Depth (km)
0
200
400
600
800
0°
5°
10°
15°
20°
25°
Distance
C
C'
CB
PMP
FC
APAP
SFC
Depth (km)
0
200
400
600
800
0°
5°
10°
15°
20°
25°
Distance
%
−1.0
−0.5
0.0
0.5
1.0

Figure 11. Figure

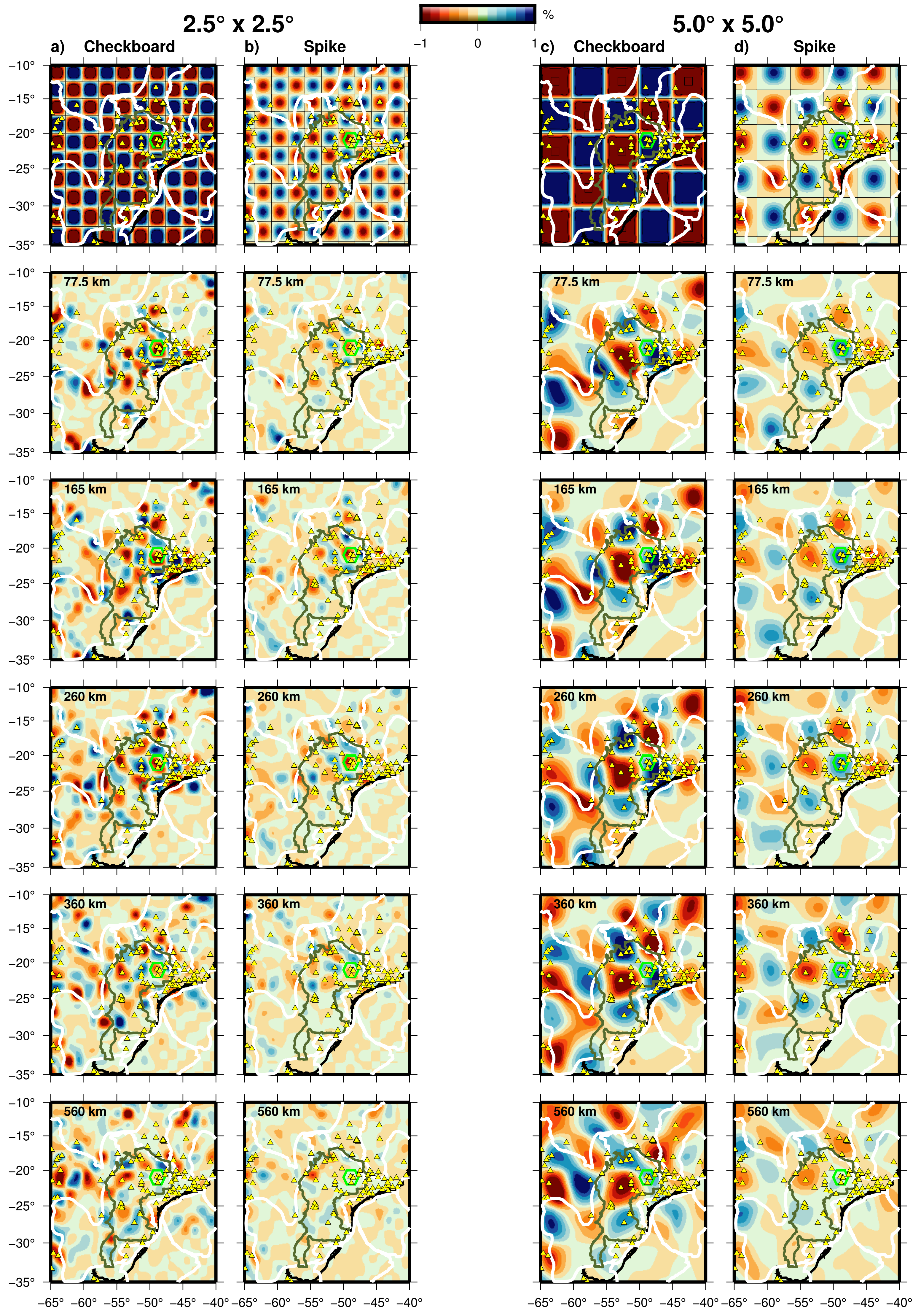

2.5° x 2.5°
5.0° x 5.0°
%
−1
0
1
a) Checkboard
b) Spike
c) Checkboard
d) Spike
77.5 km
165 km
260 km
360 km
560 km
-10°
-15°
-20°
-25°
-30°
-35°
-65°
-60°
-55°
-50°
-45°
-40°

Figure 12. Figure

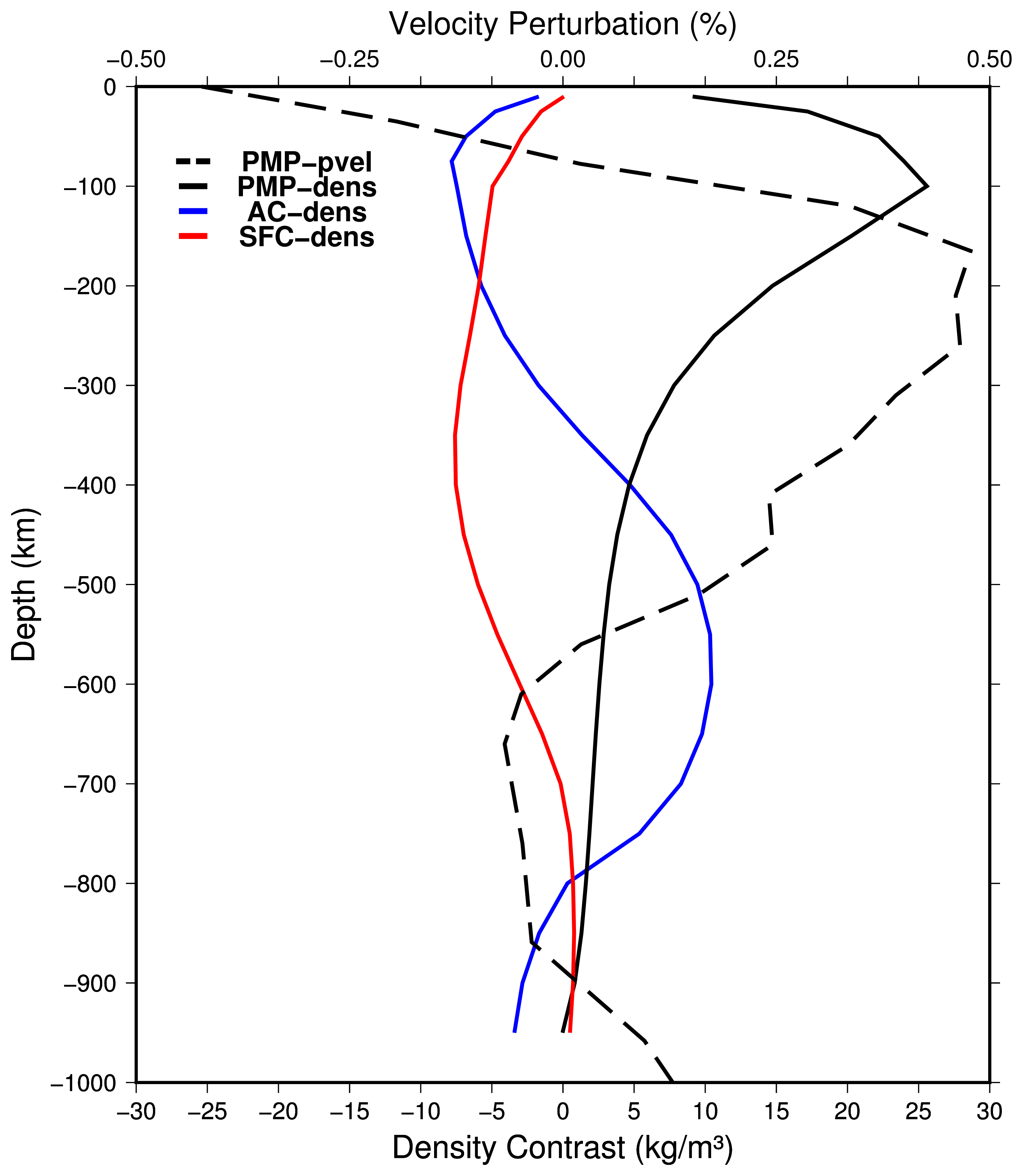
Velocity Perturbation (%)
−0.50
−0.25
0.00
0.25
0.50
0
−100
−200
−300
−400
−500
−600
−700
−800
−900
−1000
Depth (km)
PMP−pvel
PMP−dens
AC−dens
SFC−dens
−30
−25
−20
−15
−10
−5
0
5
10
15
20
25
30
Density Contrast (kg/m³)